2015

Atmospheric Effects on Radar/Ladar Detection of Seismic Activity

Michelle Frances Via
Wright State University

ATMOSPHERIC EFFECTS ON RADAR/LADAR DETECTION OF SEISMIC ACTIVITY

A thesis submitted in partial fulfillment
of the requirements for the degree of
Master of Science

By

MICHELLE FRANCES VIA
B.S. in Atmospheric Science and Climatology,
The Ohio State University, 2005

2015
Wright State University

WRIGHT STATE UNIVERSITY

GRADUATE SCHOOL

July 24, 2015

I HEREBY RECOMMEND THAT THE THESIS PREPARED UNDER MY SUPERVISION BY Michelle Frances Via ENTITLED Atmospheric Effects on Radar/Ladar Detection of Seismic Activiy BE ACCEPTED IN PARTIAL FULFILLMENT OF THE REQUIREMENTS FOR THE DEGREE OF Master of Science.

Ernest Hauser, Ph.D.
Associate Professor, Department of
Earth & Environmental Sciences

David F. Dominic, Ph.D.
Chair, Department of Earth &
Environmental Sciences

Committee on
Final Examination

Ernest Hauser, Ph.D.

Steven T. Fiorino, Ph.D.

Douglas T. Petkie, Ph.D.

Robert E. W. Fyffe, Ph.D.
Vice President for Research and
Dean of the Graduate School

ABSTRACT

Via, Michelle Frances. M.S., Department of Earth and Environmental Sciences, Wright State University, 2015. *Atmospheric Effects on Radar/Ladar Detection of Seismic Activity.*

This thesis investigates how well ground vibrations can be detected at ladar or radar wavelengths and how the atmosphere may impact the observation of such activity. First understanding atmospheric hindrances at each of these wavelengths is helpful to prioritize by those yielding best transmission results. A prerequisite to the outdoor field experiment performed for this study involves analyzing atmospheric effects characterization at six probable wavelengths using the Laser Environmental Effects Definition and Reference tool (LEEDR) developed by the Air Force Institute of Technology's (AFIT) Center for Directed Energy (CDE). These wavelengths, selected from the shortwave infrared and microwave portions of the electromagnetic (EM) spectrum, are assessed to determine which provides optimal path transmission results allowing a sensor platform at an altitude of 1525 meters to sense induced ground vibrations. Selecting an altitude just above the typical atmospheric boundary layer (BL) allows further investigation of precipitation and cloud impacts on potential path transmission. The objective of performing the outdoor field experiment is to induce surface vibrations tracked by a 12 channel geophone spread linked to a seismograph at

various locations along a horizontal path to determine if the signal can be detected by a 35 GHz radar.

The contributory goal of this research is to realize new ways of monitoring otherwise invisible illegal or terrorist-like activities for the security of this nation. Additionally, the use of LEEDR could allow the atmospheric effects measured in the microwave part of the spectrum to be scaled for various platform altitudes and applied for atmospheric correction in other parts of the spectrum such as the visible, near-infrared, infrared, or submillimeter ranges. Experimental results indicate a 35 GHz radar is optimal and capable of detecting ground vibrations across short ranges when using a retro-reflector. How well seismic activity can be detected and the impacts of estimating atmospheric transmission in various weather conditions is presented and discussed.

Table of Contents

List of Figures

List of Tables

Constants

Gravitational constant	$g = 9.81\ m\ s^{-2}$
Specific Heat of dry air, constant pressure	$c_p = 1004\ J\ K^{-1}\ kg^{-1}$
Molecular weight ratio of water to dry air	$\varepsilon = 0.622$
Latent Heat of vaporization	$l_v = 2.50 \times 10^6\ J\ kg^{-1}$
Universal gas constant	$R = 8.314\ J\ mole^{-1}\ K^{-1}$
Gas constant for water vapor	$R_v = 461.5\ J\ kg^{-1}\ K^{-1}$

(Wallace and Hobbs, 2006)

ACKNOWLEDGEMENTS

Words cannot express the amount of appreciation I have for all the key individuals who have helped this mature into a successful thesis project. A BIG thank you to Brannon Elmore, whose MATLAB expertise was priceless. Your patience and support along the way did not go unnoticed. To subject matter expert and PhD Candidate, Lee Burchett – your radar, FFT, and MATLAB guidance was truly unmeasurable. Thank you for taking the time (you didn't have to spare) to make sure the radar data was appropriately handled for best analyses. A thank you is also in order to Dr. McCrae and Dr. Basu for their suggestions on smoothing the radar data. To my WSU thesis advisors, Dr. Hauser, Dr. Petkie, and Dr. Watts your patience, expertise, guidance, and genuine support during this effort will forever be remembered. Thank you for not giving up on me! Last but not least, Dr. Fiorino, I truly can't thank you enough for all you've done to help me create and complete my master's program. Your flexibility with the hectic life, class, and work schedule made achieving this degree possible.

DEDICATED TO

To the Father, Son, & Holy Spirit for placing this challenge in my heart and allowing it to happen at the right time in my life.

To my loving, sweet, supportive, A-typical husband – the one who managed to steal my heart even after that awkward first date parting ☺ I couldn't have been blessed with a better man, husband, and best friend to stand by my side rain or shine.

To my absolutely adorable and lovable twins, Camden and Nolan – you make me happy when skies are grey! You are living proof of answered prayers and the miracle work of God.

Chapter I: Introduction

General Overview

The science of remote sensing as it relates to Earth promotes both protective and proactive measures whether it is from ourselves or our enemies. Therefore, the ability to covertly monitor ground vibrations at a specific location with either ground or space-based radar platforms has many applications in various scientific communities. The environmental, intelligence, and U.S. security communities could share a common interest in capturing otherwise invisible activities by using an asset, such as weather radar, which is readily available. From study results shared in this thesis, it is hopeful these communities gain an advanced method for protecting and proactively monitoring the earth.

Research Objectives

The overall scope of this research is to answer the following: Can we observe ground vibrations at either wavelengths typical for a ladar (~1-2μm) or radar (mm-cm)? Which of these is the optimal wavelength (ladar or radar) for observing ground vibrations, and what impact does atmospheric attenuation have on the transmission of energy in these portions of the electromagnetic (EM) spectrum as it relates to the ground vibration signal? As the distance between source and radar increases along the horizontal path, how does this impact retrieving accurate measurements? Using the Laser Environmental

Effects Definition and Reference (LEEDR) (version 4.0) atmospheric characterization software developed and maintained by the Air Force Institute of Technology's (AFIT) Center for Directed Energy (CDE), the optimal wavelength for seismic detection is identified based on scenarios created using the Wright-Patterson Air Force Base (WPAFB) Extreme and Percentile Environmental Reference Tables (ExPERT) database site *(Fiorino et al., 2014)*. Although still requiring a ground retro-reflector, this research documents why 35 GHz (~ 8 mm wavelength) is an optimal frequency/wavelength for monitoring ground vibrations at short ranges. While analysis shows both the 35 GHz (8 mm) and 10 GHz (3cm) frequencies/wavelengths are ideal, it is necessary to discuss their tradeoffs in addition to the easily accessible 35 GHz equipment.

METHODOLOGY

To begin the assessment of an optimal wavelength, transmission results from atmospheric profiles built with and without low level clouds and rain at varying rain rates are compared for six different wavelengths of interest: 1.0642 μm, 1.557 μm, 1.2 mm (250 GHz), 3.2 mm (95 GHz), 8.6 mm (35 GHz), and 3 cm (10 GHz). The results of these transmission values calculated by LEEDR (v4.0) for a 1525 meter vertical path at WPAFB ExPERT site during the summer with a 50^{th} percentile Relative Humidity (RH) from 1500-1800 local time and free of added weather (clouds or rain) are first analyzed. For further general comparison, the RH percentile is altered to 1^{st} and then 99^{th} to test extreme cases at each of the aforementioned wavelengths for the same WPAFB ExPERT atmosphere scenario. Since the 50^{th} percentile RH is essentially equivalent to an average or typical relative humidity correlation scenario for the location, this same basic set-up

was made with individual inclusion of each of the following weather parameters per wavelength: fog, stratus clouds, drizzle, or light through extreme rain rates. These outputs are then compared to finally determine the overall optimal wavelength for 'seeing through weather'.

The approach taken to experimentally answer the question, how well can seismic vibrations be detected using a 35 GHz radar, involved obtaining measurements (during clear weather conditions) in a quad located on campus at Wright State University (WSU). The radar was pointed at a retro-reflector placed directly beneath it on the ground and, at varying distances from its location, a sledge hammer was used to induce seismic vibrations. Vibrations were on a scale meant to mimic either earthquake-like or underground construction activity. A total of 12, single component geophones formed a spread connected to a seismograph and were used to trace the seismic waves as they traveled through the ground across sections of the 11 meter path. A separate geophone connected the sledge hammer and seismograph to reference a time with each impact trigger. A floating geophone connected to the radar data acquisition unit (DAQ) was moved to each impact location to attach a time stamp of when the vibrations were induced to the continuous wave (CW) radar data. Analyses is performed on obtained measurements at the varying distances between radar and sledge hammer impact sites to determine which proximity generates the clearest return.

LIMITATIONS

Although this thesis does not include an extended path experiment, such as from the top of a building, this research attempts to quantify atmospheric attenuation impacts

assuming an airborne platform. While performing studies to account for atmospheric clutter, this thesis acknowledges that ground clutter also has many impacts on Earth monitoring; however, its focus is only on atmospheric clutter.

IMPLICATIONS

Using radar presents many natural benefits including widespread distribution, highly accessible data, all weather and multi-frequency functionality, and day and night applications. In general, a radar is a valuable instrument for "seeing through clouds", but it is also ideal for monitoring precipitation events with large hydrometeors (rain, snow, sleet, hail, etc.). The latter poses a problem for understanding which vibrations received by the radar sensor are from the actual geological or human-induced event and which are from the precipitation. Therefore, LEEDR is used to characterize the atmosphere and rain events to demonstrate how it could help predict whether a radar observes rain-produced vibrations versus seismic vibrations in future studies. LEEDR also houses the ability to apply different types of rain intensity events which is useful for anticipating backscatter/phase function contributions. It is speculated that if LEEDR can help quantify these events in the radar range, then it may also be applicable to other portions of the spectrum.

In summation, consequences from this research could be beneficial for supporting: 1) Police, U.S. Border Patrol, and U.S. Homeland Security operations counteracting illegal immigration, drug cartels and trafficking, movement of terrorist weaponry, etc. through underground tunnels; 2) Earth and environmental scientists monitoring earthquake events; 3) The intelligence community monitoring or discovering subsurface structures

such as, underground tunnels, facility development and occupancy, command posts, or weaponry storage sites used by enemy countries or terrorists.

THESIS ORGANIZATION

Consisting of five chapters, this thesis is structured in a manner to first generally introduce the study performed and associated goals, and provide background knowledge on key components necessary for fully grasping the methodology, analyses of results, and conclusions. The next chapter discusses relevant previous research done, provides an appropriate background on the nature of the questions which are addressed, and bridges the gap on the necessity for further research completed in this thesis study. Chapter III describes in detail the methodology used to set-up the field experiment and perform the atmospheric simulations on each of the six wavelengths identified. Next, results and comparisons from both the outdoor experiment and LEEDR modeled scenarios are reviewed in Chapter IV. Finally, Chapter V emphasizes on the analyses of results, summarizes important conclusions on this study, and suggests areas of focus in future work.

Chapter II: Literature Review

General Overview

The purpose of this chapter is to provide significant background information to fully grasp the context and implication of questions addressed through this research. An introduction to the LEEDR software and its uniqueness for aerosol extinction consideration at the boundary layer (BL) are discussed to support its atmospheric modeling use in this study. Concepts of atmospheric attenuation including molecular and aerosol absorption and scattering and their impacts on total transmittance are fully described to promote contextual support on monochromatic transmittance at the six wavelengths investigated. To appreciate the field experiment set-up and results, background information on types of seismic waves and how they traverse through earth's materials are presented. Equipment involved to carry out the experiment are discussed as commonly used and widely accepted for obtaining reasonable results. Additionally, brief descriptions on related previous work by other scientists are mentioned along with a summary of why this thesis research is necessary can be found within this chapter.

Description

Part I:

The LEEDR software tool is a verified and validated, world-wide atmospheric characterization and radiative transfer model for the surface to 100 km that aggressively rivals similar, commonly used models such as the MODerate resolution atmospheric TRANsmission (MODTRAN) package. Its efficient capability of creating atmospheric profiles based on probabilistic surface climatology, numerical weather, surface

observations, or a standard atmosphere to investigate impacts on energy propagation at any wavelength across the EM spectrum from .35 μm (Ultraviolet) to 8.6 meters (radio frequency) via line-by-line (LBL) or 1 cm^{-1} band-averaged (Correlated-k Distribution Band Modeling method) calculations supplies both reliable and realistic output for the government (U.S. Department of Defense, DOD), private, and scientific research communities. LEEDR's inherent nature to consider location-dependent surface temperature and RH-correlated probabilistic climatology with aerosol loading within a well-mixed BL is what sets it apart from most other atmospheric radiative transfer models. It is this very reason, coupled with its ability to include optical properties of various aerosols, cloud types, and rain intensities, that LEEDR is confidently used for this thesis to accurately study atmospheric impacts on transmission at six specific wavelengths. *(Fiorino et al., 2014; Via et al., 2015).*

Using LEEDR's WPAFB ExPERT Site probabilistic surface climatology based on the 50^{th} percentile RH, summer season, and 1500-1800 local time of day for a 0-1525 meter vertical path generates realistic atmospheric profiles of important parameters including pressure, temperature, dewpoint, RH, and molecular and aerosol absorption and scattering. The correlated, probabilistic nature of the ExPERT database for the 573 land locations housed within LEEDR allows users to define an environment based on extremity of moisture conditions. Although a wide range in RH percentiles are available for selection, the 50^{th} percentile represents an average or typical setup for the site selected. Perhaps most importantly, in all cases the surface parameters are correlated in such a way they could truly, physically occur at the site. This is quite unlike the standard

atmosphere. The U.S. 1976 Standard Atmosphere is based on 45° North Latitude with conditions that may not be physically representative for any given location. Thus, the ExPERT database allows an added level of accuracy right from the start through surface parameter correlation based on 30 years of climatology for each location. Since the ExPERT database can be specific to season (summer/winter) and time of day, this modulates an appropriate default BL height to apply in the resulting profile. Therefore, the background atmosphere used in this research has a LEEDR-defined BL at 1524 meters. The same vertical path set in each clear and weather event scenario goes from the surface to 1 meter beyond the BL definition (1525 meters) to consider impacts at an altitude which could be within a low level cloud and not simply at its base. Above the BL, LEEDR reverts to a standard regional upper-air atmosphere. *(Fiorino et al., 2014; Via et al., 2015).*

Another unique feature of LEEDR's ExPERT atmosphere profile definition is its application of standard lapse rate equations in combination with probabilistic surface climatology. More directly, above the surface, LEEDR allows standard rates of decrease with altitude to be independently applied to surface temperature and dewpoint temperature. Equations 1 and 2 below define the standard dry adiabatic and dewpoint lapse rates respectively and come directly from *Fiorino et al. (2014).* Once air becomes saturated, the lapse rate in temperature is defined by the saturated adiabatic lapse rate and shown in Equation 3 (*Fiorino et al., 2014).* As discussed in *Wallace and Hobbs (2006),* because the latter rate is highly temperature and pressure dependent, and these parameters

alter with height, the rate of change in temperature is no longer persistent in moist air. *(Fiorino et al., 2014; Wallace and Hobbs, 2006).*

$$\left(\frac{dT}{dz}\right)_{dry} = -\frac{g}{c_p} = -9.8K \cdot km^{-1}. \quad (1)$$

$$\left(\frac{dT_d}{dz}\right) = -\frac{g}{\varepsilon l_v}\frac{T_d^2}{T} \approx -1.8K \cdot km^{-1}. \quad (2)$$

In equations 1, 2, and 3: T is temperature, T_d is dewpoint temperature, z is height, g is the gravitational constant, c_p is the specific heat of air at constant pressure, ε is the ratio of the molecular weight of water over the molecular weight of dry air, and l_v is the latent heat of vaporization of water.

$$\left(\frac{dT}{dz}\right)_{moist} = -\frac{g}{c_p}\frac{1 + l_v \, w_s / RT}{1 + l_v^2 \, w_s / c_p R_v T^2}, \quad (3)$$

where w_s is the saturation mixing ratio of water, and R_v is the moist-air gas constant. (*Fiorino et al., 2014).*

An important take away from the above lapse rate discussion is the possibility for saturation and even supersaturation to occur within the BL allowing low level cloud types (specifically, fog, stratus, and cumulus) to form within the vertical path defined in this study. Generally speaking, with the presence of cloud condensation nuclei (CCN) or water-soluble aerosols, the stage is set for clouds to form at a level where the RH is greater than 100% (i.e. when supersaturation occurs). Realizing the important physical

role these lapse rates play in generating accurate atmospheric profiles, especially in terms of RH and defining saturation levels, a deeper appreciation develops for the kind of realistic propagation impacts LEEDR is capable of modeling. Based on these definitions, as RH increases with altitude within the BL, there is a direct relationship on aerosol size distributions that the standard atmosphere model fails to depict. When more moisture is present in the atmosphere, water-soluble aerosols grow, often times forming clouds which can eventually lead to rain and, no matter what stage of development, all of which can attenuate the transmission of energy depending on the wavelength of interest. *(Fiorino et al, 2014; Wallace and Hobbs, 2006; Ahrens, 2003).*

For the purposes of this research, the following six wavelengths are investigated: 1.0642 µm, 1.557 µm, 250 GHz (0.119917 cm), 95 GHz (0.315571 cm), 35 GHz (0.856549 cm), and 10 GHz (2.997925 cm). Each of these can be referenced in the EM spectrum shown in Figure 1 as they relate to one another in the ladar, millimeter wave, or radar regimes. The remote sensing community may use the term ladar or lidar interchangeably to reference the same portion of the spectral regime. LAser (or LIght) Detection And Ranging instruments, where 1.0642 µm and 1.557 µm are located, are used like a pulsed radar to paint a picture (via range calculations) of elevations on a surface such as the earth *(Rees, 2001).*

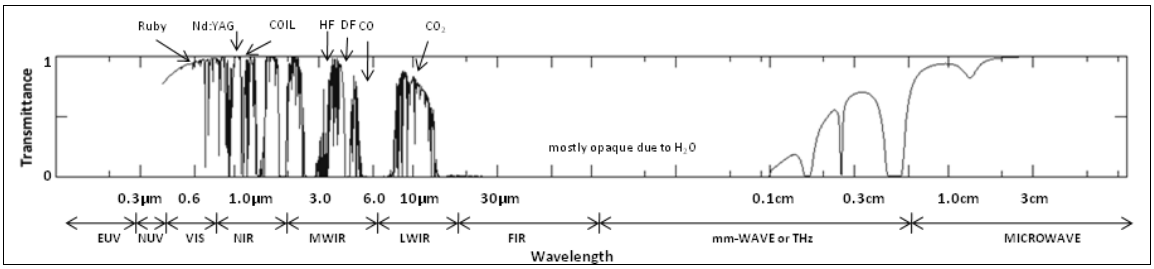

Figure 1. This broadband, total transmittance plot for a vertical path describes how various portions of the EM spectrum can be referenced depending on associated wavelengths. The additional notations for wavelengths between the VIS to LWIR capture common laser wavelengths. This figure was taken from *'Introduction to Laser Weapons Systems'* (Figure 8.7) with permission from authors, Dr. Glen P. Perram and Dr. Steven T. Fiorino. *(Perram et al, 2010).*

Since the term transmission with respect to the atmosphere is a primary focus throughout this research and analyses, especially in Part I, a solid understanding of the term is important. Occasionally, transmission and transmittance are used to refer to the same concept. Although there is a small technical difference between the two where transmittance is effectively normalized to 1 and transmission is the same fraction described as a percentage, for simplicity purposes transmission is the term of choice in this paper *(Fiorino, 2015).* Transmission in general terms relates the intensities of monochromatic energy that passes through a medium to the total energy incident and is explained mathematically by Beer's Law over a given path length:

$$t(x) = \frac{I(x)}{I_0} = \exp^{(-\beta_e x)} . \tag{4}$$

Where $I(x)/I_0$ refers to transmission, β_e is the total extinction coefficient or the sum of the absorption and scattering coefficients (β_a and β_s) and is strongly wavelength-dependent, and x is the length of the path the energy is being transmitted across *(Petty,*

2006). As transmission approaches 1 (or 100%) for a given path and wavelength, the maximum intensity of energy is passing through the atmosphere and can be thought of on a spectral transmission plot as an atmospheric window.

As Beer's Law suggests, the degree of severity an atmosphere's moisture profile, molecular constituents, and aerosol content has on the total extinction of energy, especially when combined with weather phenomena like clouds or rain, depends heavily on the wavelength of interest. Spectrally, the size of a wavelength relative to the atmospheric particulate it interacts with strongly dictates the amount of absorption and scattering that occurs *(Fiorino, 2015).* Figures 2 and 3 below further demonstrate this fact by first highlighting transmission effects of individual components in clear air scenarios and then by focusing on just the optical property impacts of individual cloud types or rain intensities (without considering molecules or aerosols) across a broad spectrum. These two figures come together in Chapter IV by providing collective impacts which suggest important wavelength-dependent strengths and weaknesses.

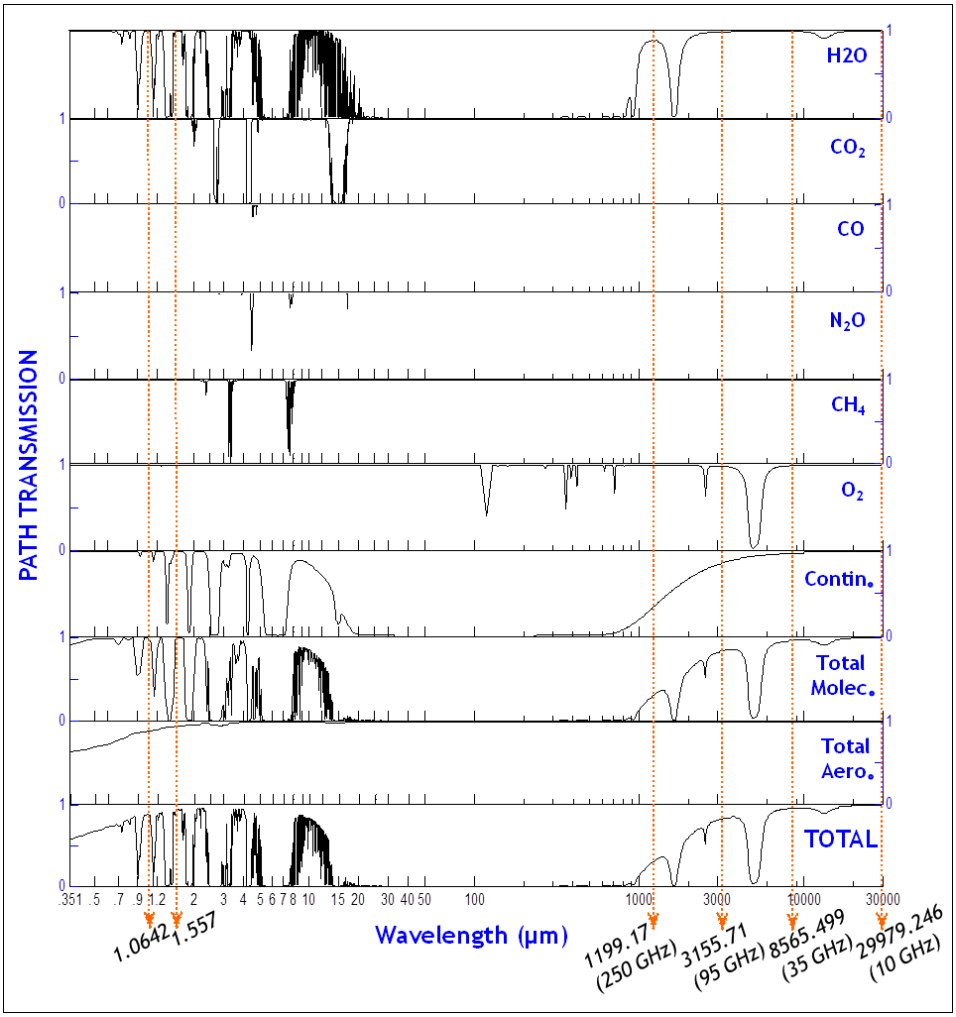

Figure 2. Individual per molecular constituent transmission plots along a 1525 meter vertical path through the boundary layer show overall contribution to total atmospheric transmission. The six wavelengths studied in this thesis are highlighted to reference attenuation impacts at each.

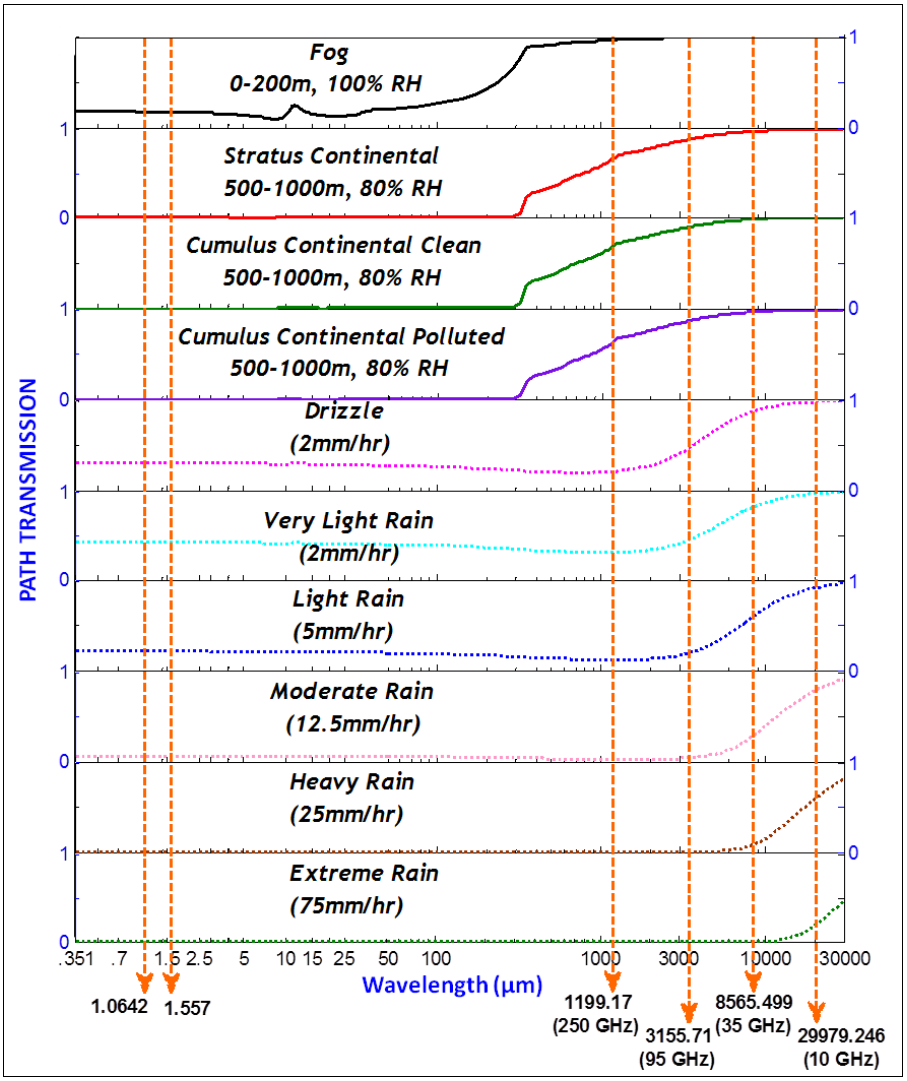

Figure 3. Individual cloud and rain type transmission plots along a 1525 meter vertical path through the boundary layer. Plots consider only optical property contributions for each weather type to demonstrate pure cloud or rain impacts spectrally. The six wavelengths studied in this thesis are again highlighted to reference attenuation impacts at each.

The individual molecular constituents shown above are considered the major contributors to attenuation in the 1525 meter vertical path defined by the clear air, WPAFB ExPERT atmosphere studied. From top to bottom of the figure, water vapor through water vapor continuum considers where each molecular constituent's absorption

hindrances occur spectrally. The total molecular path transmission is determined based on the product of each constituent's molecular absorptions per wavelength as well as the product of molecular scattering. As observed in the total molecular plot, molecular scattering is responsible for inhibiting transmission for wavelengths less than roughly 0.5 μm *(Petty, 2006)*. The total aerosol plot considers only aerosol scattering and absorption effects across the same spectrum; from this it is evident the contribution from aerosol scattering on impeded transmission is largely at wavelengths below roughly 4 μm. Since aerosol effects are then minimal beyond this, LEEDR stops accounting for their impacts at 40 μm and assumes a transmission of 1 (or 100%) *(Fiorino et al., 2014)*. The final plot for total transmission is a per wavelength product of all individual component's (molecular and aerosol absorption and scattering) transmission values *(Petty, 2006)*. Therefore, by viewing molecular and aerosol impacts individually and then collectively, it becomes easier to identify specific reasons for drops in overall transmission. For example, although both laser wavelengths are in transmission windows, the aerosols are predominantly responsible for attenuating light. Comparatively, 1.0642 μm suffers more from aerosol extinction, which is why 1.557 μm is a better choice laser for clear air propagation. Likewise, at 250 GHz the water and, chiefly, the water vapor continuum are what give the final transmission shape in that region.

When comparing Figure 2 with Figure 3, an important point for consideration while setting up rain event scenarios in this study becomes prevalent: rain attenuates light propagation more strongly than water vapor in almost all cases and wavelengths in the spectrum shown. The only exceptions are drizzle and very light rain at 10 GHz where the

transmission is already nearly perfect. It is due to this concept there was no need to alter the default RH value on LEEDR's Ground Level tab during rain event transmission comparisons. Another aspect Figure 3 brings to light refers to the slight dip observed in transmission at 250 GHz compared to surrounding wavelengths for drizzle through light rain intensities. This decrease in transmission deals with Mie scattering and extinction efficiency (i.e. the total impediment based the sum of scattering and absorption) *(Wallace and Hobbs, 2006)*. Mie scattering occurs when atmospheric particulate have a size that is either comparable to or greater than the wavelength of light *(Petty, 2006)*. LEEDR uses a 2mm/hour rain rate for drizzle and very light rain and 5mm/hour for light rain where the latter two use a Marshall-Palmer size distribution based on modal raindrops of 1-5 mm in size *(Fiorino)*. This is key for substitution into the size parameter equation (5) below which provides a way to relate to extinction efficiency *(Wallace and Hobbs, 2006; Petty, 2006)*.

$$x = \frac{2\pi r}{\lambda} \tag{5}$$

Where r is the radius of the particle and λ is the wavelength of light.

The size range of 1-5 mm corresponds to 300-60 GHz (respectively) which by Equation (5) means if λ were also 300-60 GHz then the ratio of $r/\lambda = 1$ making the size parameter (x) ~6. In *Petty (2006)*, this size parameter value is where the extinction efficiency is at its greatest. Thus, at 250 GHz there is a dip in transmission owing to this extinction peak.

Since Mie scattering has been introduced, it is beneficial to also briefly discuss its subset, Rayleigh scattering. Effects of Rayleigh scattering are observed in spectral regimes when the propagation wavelength is ~10 times or more larger than the atmospheric particulates it encounters. In this case, the intensity of light scattered is directly proportional to λ^{-4} making this parameter easier to calculate analytically than computationally intensive Mie scattering. Comparing these two scattering theories, it is evident that Mie scattering plays an important role in accessing the effects of aerosols on visible light, and clouds and rain on longer, microwave wavelengths such as those used in weather radars. *(Petty, 2006; Wallace and Hobbs, 2006)*

Based on the study discussed in *Fiorino et al, 2010*, and in addition to 1.0642 μm & 1.557 μm being common laser wavelengths, 250 GHz and 95 GHz were included in the microwave regime with 35 GHz and 10 GHz for atmospheric attenuation impacts research. Therefore, this thesis is partially an extension of the vertical path transmission comparisons made in both clear air and clouds or rain scenarios discussed in this "Worldwide uncertainty assessments of ladar and radar signal-to-noise ratio performance for diverse low altitude atmospheric environments" publication in the *Journal of Applied Remote Sensing*. Although this thesis strictly uses LEEDR for output comparisons, it should be noted the CDE's High Energy Laser End-to-End Operational Simulation (HELEEOS) model encompasses LEEDR code which it relies on as the backbone for all atmospheric propagation calculations. Thus, comparisons and references to publication output is reasonable. That said a few points about the scenario set up used in this thesis and those in *Fiorino et al, 2010* are worth discussing. The same vertical path from the

surface to 1525 meters is considered but only with respect to the WPAFB ExPERT site for the specific 1500-1800 local, summer timeframe as opposed to a world-wide assessment based on temperature, moisture, and pressure daily averages per location. Three of the weather events studied here are also assessed in the publication: fog (0-200 meters), stratus (500-1000 meters), and heavy rain. The latter is what prompted this thesis to take an advanced approach by considering more appropriate RH values at the surface in low level cloud scenarios rather than simply relying on 50^{th} percentile correlations where the atmosphere is assumed free of weather events. Using the Ground Level tab to alter the default surface RH to 100% for fog and 80% for stratus and cumulus scenarios manually forces LEEDR to apply the dry adiabatic and saturated adiabatic lapse rates at appropriate levels supporting where water-soluble aerosols grow in modeled cloud development. As already mentioned and further supported by *Fiorino et al, 2010*, modeling water vapor profiles and aerosol loading correctly is imperative for understanding true LBL transmission impacts. For this reason, one can expect the methodology followed in the next chapter to capture results on the optimal wavelength for observing ground vibrations that apply even during potential cloud or rain events. *(Fiorino et al, 2010).*

PART II:

Atmospheric science, seismology, and remote sensing are all inter-related geophysics disciplines, and the science behind each of these fields combine for the research performed in this thesis. Part II of this study involves a seismic array coupled with an active, CW radar placed at one end of the path. Seismic equipment such as geophones

and seismographs are generally used to monitor vertical profiles of the underlying surface for typical Earth geophysical applications including, but not limited to: determining soil type based on the speed at which seismic waves travel through the layers, locating aquifers, determining rock strength for supporting new buildings or bridges, finding oil reservoirs, locating buried historical sites or underground tunnel systems, and more traditionally, to monitor overall seismic activity of Earth near fault lines probable of earthquakes. The aim of research in this thesis is to target whether or not induced seismic activity can be observed by radar compared to truth measurements obtained via a 12 channel seismic array. If successful, novel applications to border security and military monitoring could surface.

In 2012, Sandia National Laboratory (SNL), a Federally Funded R&D Center (FFRDC) headquartered in Albuquerque, New Mexico, released news on a research project done to investigate the use of seismic refraction and reflection to detect underground tunnels. The SNL is operated by a contracting company largely supporting various government entities including the DOE and DOD. In a similar research project with results published in 2010, Sandia performed studies with the same ultimate goal but evaluated both active and passive seismic detection practices as well as passive EM sensors in hopes their combination of results could remove the blinders on underground activity. The inclusion of studies using a passive EM sensor makes an attempt to uncover irregularities associated with underground facilities by looking for common signals for general operation such as those detectable from 60 Hz overhead lighting. In both projects, results describe the many complexities involved with reaching the goal to detect

underground tunnels; some of which include signal-to-noise ratio challenges, the need to initially understand surrounding ambient signals to better account for their removal, subsurface refractivity or reflectivity changes due to the presence of water in some capacity, and lastly, understanding velocity of seismic wave returns and how velocity inversions can hide subsurface layers or objects. Although an underground tunnel would be the expected anomaly, it is the ability to differentiate it from other unexpected anomalies (both above and below the ground) through the use of remote sensing techniques that drives the need for further research. From the field experiment performed in this thesis, comparative results using an active EM sensor with a seismic array will provide another perspective for achieving the overall goal to protect U.S. security. *(Sandia News Release, 2012; Sandia Project Report, 2010;Reynolds,2011).*

Scientific theory and background supporting instrumentation used to complete the field experiment are discussed next. To take accurate measurements, a source with controllable energy capable of generating significant ground motion was required. A sledge hammer swung to strike a steel plate is a common, widely accepted, inexpensive impact trigger for near surface refractivity surveys such as the one expressed. However, its correct use in each shot record generated is imperative. To ensure all shot records have a source that's clean and consistent in magnitude, Dr. Hauser was the sole operator responsible for inducing a single strike per record. *(Reynolds, 2011)*.

The vertical component geophone instruments used in an array are crucial to measure the seismic wave as it passes through the subsurface path. Each of the 12 used in this field survey refer to a specific trace recorded in the seismograph and can provide insight

on the types of waves encountered based on the voltage measured. These individual instruments are linked together via cables to create a spread or array outlining the experiment path. Individual geophones consist of a freely-moving coil with an associated tension giving a resonant frequency of 4.5 Hz. Thus, these geophones are able to track low frequency movements when placed in the ground via their metal spike. As waves from the induced ground vibrations pass a geophone, the magnetic casing surrounding the coil and connected to the spike is displaced in sync with the ground's response. The coil inside begins to oscillate with respect to this exterior movement and an electrical voltage in terms of velocity is recorded. *(Reynolds, 2011).*

The types of waves able to traverse the underlying surface from induced vibrations can be broadly categorized as either body waves or surface waves. Body waves are capable of traveling more deeply through the earth, but only P-waves are able to travel through underlying materials in either a solid or liquid state. S-waves are restricted to transmitting only through solids. Conversely, a surface wave travels as its name suggests; near the earth's surface and, regardless of the sub-category type of wave, may only traverse through solid mediums. Therefore, both main category waves can be further referenced through associated sub-types. Compressional (P-waves) and shear (S-waves) waves are types of body waves, and Rayleigh and Love waves are types of surface waves. Focusing on body waves, the relative movement of the earth materials with respect to the wave propagation can be further described. P-waves compress and release the material parallel with direction of wave propagation. However, S-waves will move materials orthogonally to the direction of wave propagation. These body waves can also

be reflected or refracted within the subsurface layers causing directional changes in propagation. In general, refraction occurs when the seismic wave encounters a new subsurface layer encompassing a different (greater) propagation velocity from the layer above due to a change in material structure or composition. In certain conditions, critical refraction can occur where the wave will actually traverse along the border separating the two different underlying mediums at the increased rate associated with the more dense, second (lower) layer *(Reynolds, 2011).* A basic understanding of the various types of subsurface waves which could be encountered and how they may propagate during an experiment helps to identify the more appropriate seismic equipment for a successful data collection. *(Reynolds, 2011).*

To address the remote sensing application of this study, the radar equipment will be discussed next. Radar stands for RAdio Detection And Ranging and has many uses in both the civilian and government arenas, ranging from police departments to detect speed violators, weather monitoring, and terrain mapping from space-based platforms. An advantage of using radars in remote sensing applications is that it can be used day or night as it is not dependent on illumination from the sun to make detections. Radars can be used actively as CW or pulsed, or passively depending on the mission. In this research, the radar was in an active CW mode, which supports the need for a separate floating geophone connected to the radar DAQ to place an impact time stamp on the received radar data. As previously mentioned during the introduction to lidar, active mode radars are unique in their ability to determine both a range to target in addition to the energy received *(Rees, 2001).*

The 35 GHz Ducommun homodyne CW radar (Model # SRF-35120610-01, refer to Appendix B) used in this study can be thought of in the same way a Michelson Interferometer works to determine the motion of a mirror *(Petkie, 2015)*. Essentially, the induced ground vibrations cause a change in the length of one of the arms (paths) of the interferometer that modulates the output of the interferometer. The incoming or received signal is split into two beams of energy and sent through individual mixers. The output of the mixers (IF1 and IF2 of Figure 4) are referred to in radar as the In-phase (I) and Quadrature phase (Q) signals and each provide information on the motion of the target. The channels in combination can provide directional information on the received signal (i.e. if the object or wave in this case is moving toward or away from the radar unit).

Figure 4 comes from Ducommun Inc. and depicts the radar module, with a carrier frequency of 35 GHz (f_0), used in the field experiment. The beam goes out to the ground beneath and reflects off the retroreflector back to the receiver. This returned signal then becomes two sets of data where one is phase shifted 90° from the other and the two signals are then referred to as I and Q. As shown, both I and Q go through separate amplifiers (SR560 Low-Noise Voltage Preamplifiers) where eventually the two signals are processed in terms of voltage along a time series. The time variation in the measured voltages represents the ground movement via the Michelson Interferometer, or alternatively, Doppler shift. *(Petkie, 2015; Ducommun, 2015; Petkie et al., 2008).*

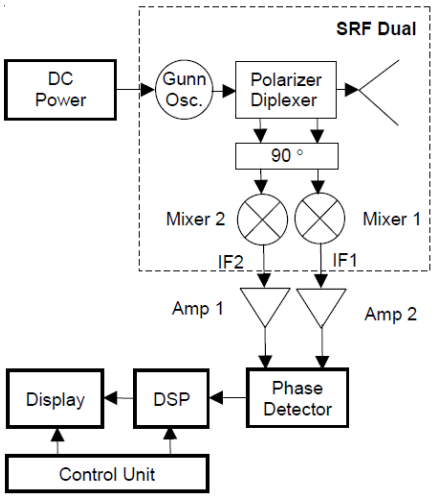

Figure 4. Depiction of a 35 GHz CW radar in conjunction with preamplifiers and processing components. *Compliments of Ducommun Inc. Bulletin No. SRF & SRR.* Refer to Appendix B.

The radar data (both radar channels and a synchronization geophone located at the impact site) were simultaneously collected at a 100 kHz rate (10 microsecond sample rate) using a USB National Instruments DAQ for a duration of 5 seconds. Data collection was manually triggered an instant before impact.

Post processing on radar data can involve Fast Fourier Transform (FFT) calculations to transform the voltages recorded with respect to time to be magnitudes with respect to frequency. MATLAB is a useful and efficient tool to perform these calculations. Thus, performing the FFT provides a way to view radar output from a different perspective by identifying main peak frequency and even smaller peaks received in the data collection. *(MathWorks, 2015).*

SUMMARY

Key concepts discussed throughout this chapter provide significant support for the methodology used and the credibility of results obtained. Therefore, Chapters III and IV set the final stage for vital conclusions made in Chapter V which are assertively made based on the preceding theories summarized.

Chapter III: Methodology

General Overview

The research performed for this study took place in a two-part approach: 1) LEEDR scenarios were created to assess atmospheric impacts for each of the six identified wavelengths (1.0642 µm, 1.557 µm, 250 GHz, 95 GHz, 35 GHz, and 10 GHz) to capture key performance challenges due to attenuation, and 2) The readily available 35 GHz radar was employed in an outdoor field experiment to determine capability to detect induced ground motion. Part I of the research approach allowed comparative analyses between wavelengths on the extremity of weather conditions each could handle before transmission was significantly degraded. It was essential to initially investigate how a 35 GHz radar would perform in various weather conditions prior to use in Part II. Therefore, the ultimate goal was to conduct the outdoor field experiment at a wavelength which offered flexibility for operation under a wide range of weather conditions. The following subsections describe in detail this two-part research approach.

PART I – LEEDR-modeled Attenuation

To perform the LEEDR analyses, transmission results per wavelength were assessed under two separate categories. The first accounted for the atmosphere under clear conditions, but varied the relative humidity (RH) percentiles: 1^{st}, 50^{th}, and 99^{th}. The second category used the same background atmosphere (with 50^{th} RH percentile), but added individual weather conditions such as fog and rain. The LEEDR model provided an estimate of how well each wavelength performed under these different conditions and helped to quickly highlight which would likely see through the most types of weather

proving more advantageous operationally. Subsequent paragraphs outline the steps taken to gather the wavelength-dependent results for comparison.

The background atmosphere was first defined in LEEDR and used within both categories' calculations. Since the outdoor field experiment was to be performed on WSU's campus, the surface climatology encapsulated in the WPAFB ExPERT Site was deemed most realistic due to proximity to mimic the study location's typical atmospheric conditions. As supported in Chapter II, it was imperative to identify a representative background atmosphere to capture truthful transmission results. Figure 5 below depicts the actual quad location from the experiment and the appropriate setting on the Location tab within the LEEDR Graphical User Interface (GUI).

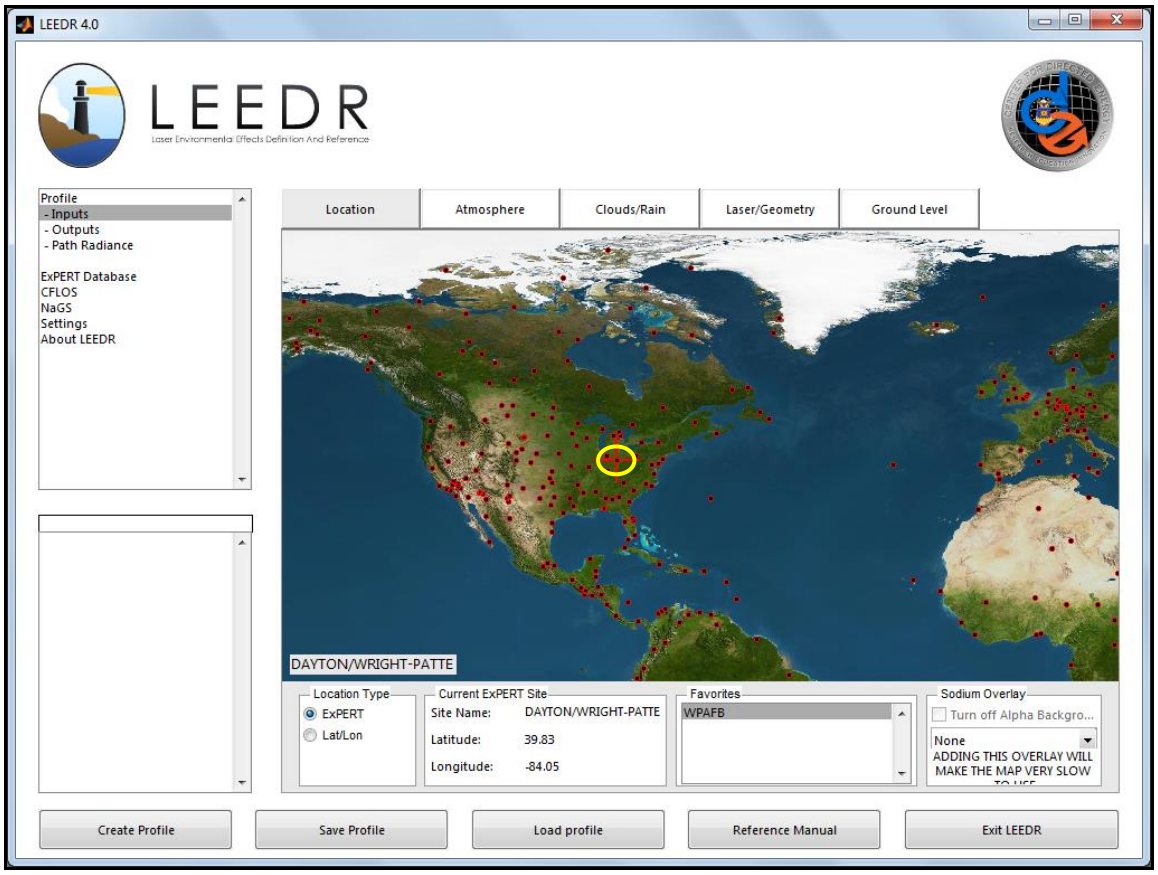

Figure 5. *(Top)* Experiment location on WSU's campus. Equipment set-up within yellow circle in front of Fawcett Hall. *Satellite view compliments of Google Maps*. *(Bottom)* Equivalent LEEDR location (WPAFB ExPERT Site) for background atmospheric profile.

The field experiment was performed in the afternoon on 24 July 2013 and prompted the appropriate settings shown on LEEDR's Atmosphere and Laser/Geometry tabs in Figure 6. To perform the first category's analyses per wavelength, a summer ExPERT atmosphere in the 1500-1800 local time block with the Global Aerosol Dataset (GADS, a 5° x 5° worldwide gridded dataset) model was used with a 50^{th}, 1^{st}, or 99^{th} RH percentile bin over a 1525 meter vertical path to encompass full BL effects (*Fiorino et al, 2014*). The 50^{th} percentile RH was applied first in the atmospheric settings for each of the wavelengths to understand average or typical moisture correlation impacts. These

comparisons were then followed-up with a 1st percentile RH setting at each wavelength and then a 99th. Although percentile settings of 5, 10, 20, 80, 90, and 95 were also available within LEEDR, the 1st (driest) and 99th (wettest) represent moisture extremes for a given location. Collectively, these three cases allowed assessment of individual wavelength performances across the wide range of moisture conditions. The purpose for choosing a path length just beyond the model's inherent BL (where hygroscopic aerosols swell in size allowing cloud formation) of 1524 meters for the selected season and time of day was two-fold. First, it set the appropriate upper boundary for the addition of rain events which originate within a cloud deck as opposed to at or below the cloud base; second, it adhered to the consideration of atmospheric attenuation if an instrument at one of the six wavelengths was placed on an airborne aircraft platform. In the latter instance, and with the exception of cumulus cloud scenarios, it was assumed an aircraft would travel just below a cloud deck to better interrogate the earth's surface, and therefore, be completely immersed within each rain condition.

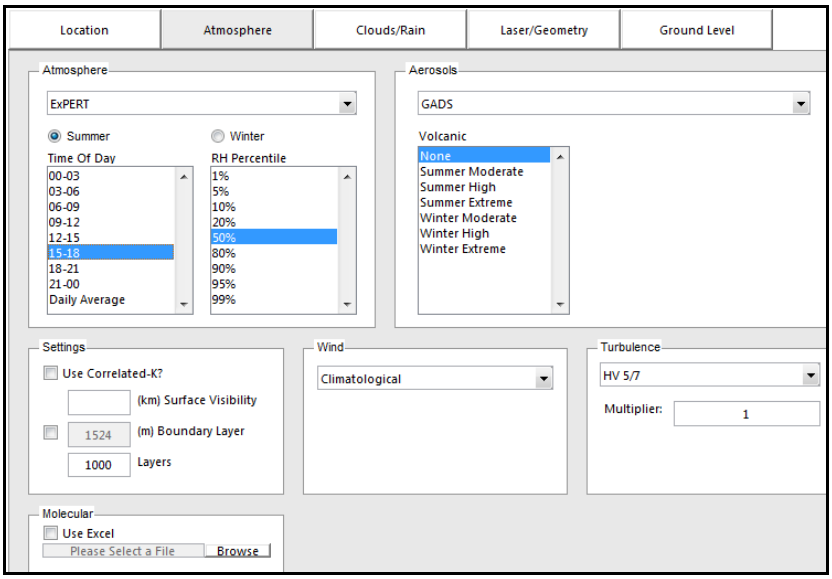

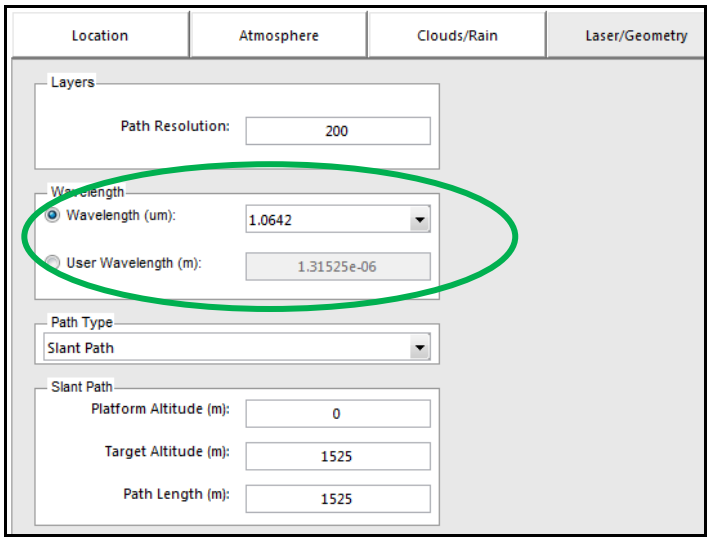

Figure 6. LEEDR Atmosphere *(top)* and Laser/Geometry *(bottom)* tab settings made to create the background atmospheric profile per wavelength considered. The 1524-meter BL definition was a default setting, and the Use Correlated-K checkbox was left unchecked to instruct LEEDR to perform LBL calculations as opposed to band-averaged. Each line or wavelength is set on the Laser/Geometry tab as shown.

Once each of the six wavelength's transmission results were documented according to the three RH percentile WPAFB ExPERT atmospheres, the second category's atmospheric settings were addressed. The purpose of this next category was to test the individual addition of various weather phenomena which could limit transmission results per wavelength. As previously stated, since the 50th percentile represented an ordinary RH correlation scenario for the location, season, and time closest to matching completion of the field experiment, this setting remained static per profile created. Therefore, in addition to the same background summer, 50th percentile, 1525-meter vertical path, WPAFB ExPERT site atmosphere, explicit settings for modeling cloud or rain attenuation impacts were also required. At each wavelength, individual weather parameters under investigation included: Fog (0-200 meters), Stratus Continental (500-

1000 meters), Cumulus Continental Clean (500-1000 meters), Cumulus Continental Polluted (500-1000 meters), Drizzle (2 mm/hr), Very Light Rain (2 mm/hr), Light Rain (5 mm/hr), Moderate Rain (12.5 mm/hr), Heavy Rain (25 mm/hr), and Extreme Rain (75 mm/hr) *(Hess et al., 1998)*. The cloud varieties investigated were carefully chosen since only low level cloud types could physically appear within the 0-1525-meter path. Consequently, the rain rates were chosen because they could occur within either one or both the Stratus or Cumulus Continental cloud types. Heavy and Extreme Rain rates typically occur during a thunderstorm event, which again allowed for an assessment of extreme case scenarios per wavelength. In general, the cloud and rain types modeled provide a decent variation in water droplet sizes as this impacts the three spectral regimes studied (laser, millimeter, and radar).

As shown in Figure 7 below, LEEDR's Ground Level and Clouds/Rain tabs were used to adjust the surface RH and/or include cloud or rain optical properties respectively. It was imperative to correctly account for RH, and consequently water vapor profiles, when clouds were included within the vertical path to realistically capture transmission impacts. When assessing each wavelength's performance through fog, the surface RH was set to 100% on the Ground Level tab to ensure LEEDR used the saturated adiabatic lapse rate at the start of the path as opposed to the dry adiabatic lapse rate under ordinary (clear) conditions. Therefore, without manually adjusting the surface RH from climatology, the temperature and dewpoint profiles would not be representative for a layer of fog occurring from the surface to 200 meters. Likewise, while studying stratus and cumulus cloud degradations on propagation performance, the RH was set to 80% on

the Ground Level tab to allow temperature and dewpoint profiles to demonstrate saturation at the cloud base (500 meters).

To add the cloud type or rain rate studied per wavelength, the appropriate selection was made from the Weather Type dropdown on the Clouds/Rain tab. An upper and lower altitude boundary was required for LEEDR to calculate condition impacts in the correct portion of the path. Although the fog and stratus cloud types were placed within realistic altitude boundaries, the cumulus cloud types were somewhat artificially placed. Cumulus clouds generally do not occur as low as 500 meters and are much thicker than stratus type clouds. Yet the decision for placement within the same defined boundaries as the stratus was essential from a modeling perspective. Knowing an aircraft carrying instrumentation specific for interrogating the earth's surface would not fly within a cloud to achieve this goal, a cumulus or strato-cumulus cloud may be hit by the beam from an oblique angle. Thus, considering their impacts seemed vital as well. All rain intensities modeled were set to occur through the entire surface to 1525 meter vertical path.

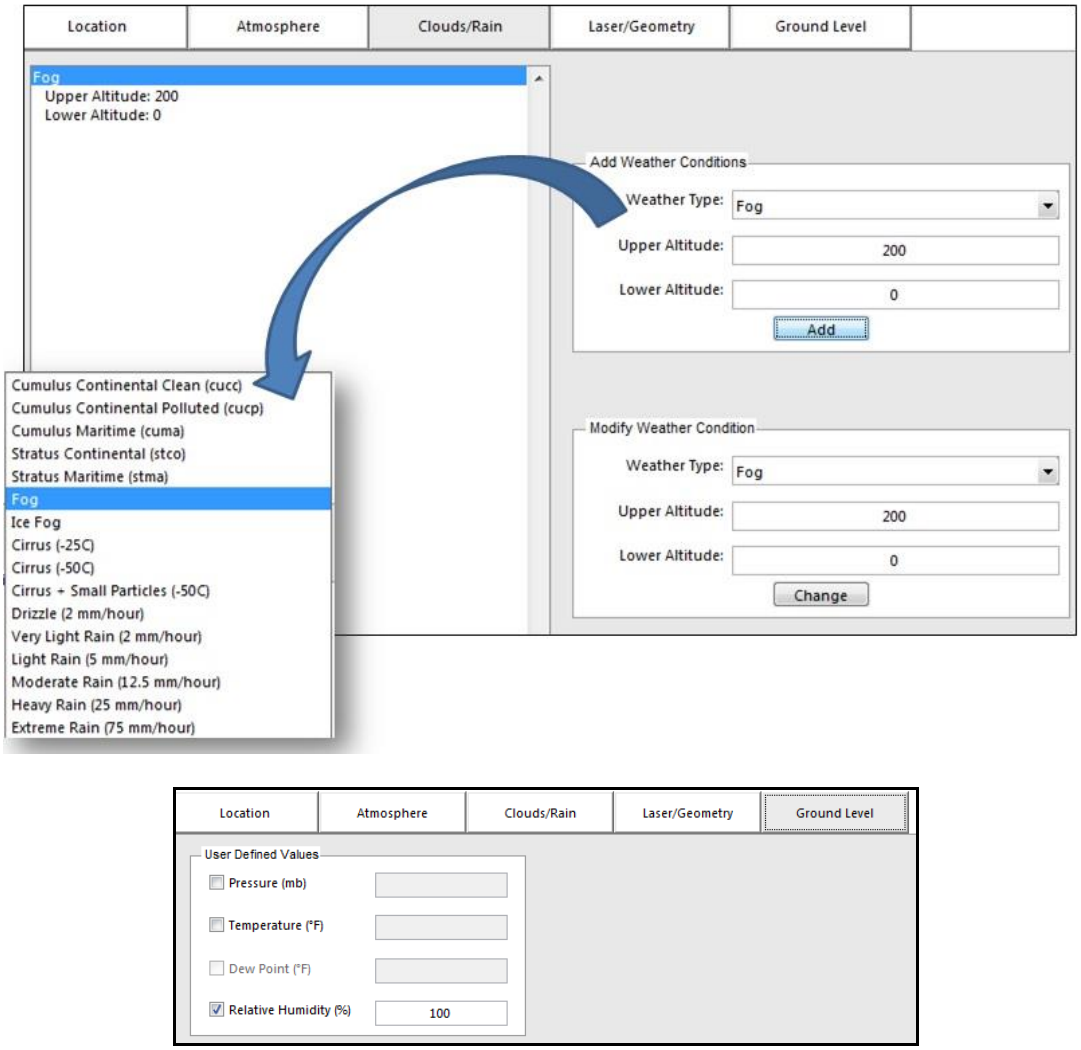

Figure 7. LEEDR Clouds/Rain *(top)* and Ground Level *(bottom)* tab settings were used to create scenarios including clouds or rain for the second category's transmission assessments. Each cloud type or rain rate was set on the Clouds/Rain tab via the weather type dropdown with associated upper and lower condition boundaries. The Ground Level tab's RH percentage field was only edited for use with cloud scenarios.

During both categories' transmission analyses, calculations were performed LBL to obtain accurate results per wavelength studied. As shown in Figure 6, the Use Correlated-K checkbox was left unchecked on the Atmosphere tab to instruct LEEDR to perform LBL calculations as opposed to band-averaged. Since six wavelengths were explicitly

considered for this study, transmission results occurring at those precise lines were desired. More importantly, it was assumed the instrument used for seismic detection would be monochromatic. Running LEEDR under Correlated-K could have under/overestimated or smoothed transmission impacts making results unreliable for comparative purposes. Again, the overall goal for Part I was to use the LEEDR model to capture wavelength performance considering various atmospheric conditions. Completion of all steps outlined above provided stable results to accomplish that goal.

PART II – OUTDOOR RADAR FIELD EXPERIMENT

This portion of the research involved outdoor deployment of a continuous wave (CW) 35 GHz radar on WSU's campus (see Figure 5) to test its capability to detect induced seismic activity. Prior to full outdoor execution, preliminary indoor lab tests with the radar unit, retroreflector, small block of wood, and hammer were conducted to validate the experiment concept. Initially, the indoor tests suggested a fair amount of noise cluttered the final returned signal and required adjustments to DAQ amplifiers. Therefore to further minimize signal confusion, this summer afternoon (24 July 2013) experiment took place in absence of rain or inclement weather to ensure the received signal was from the true induced source. The following describes how the outdoor experiment was performed, and Figure 8 is a schematic of instrumentation set up. Additionally, photos taken of equipment and experiment execution are included.

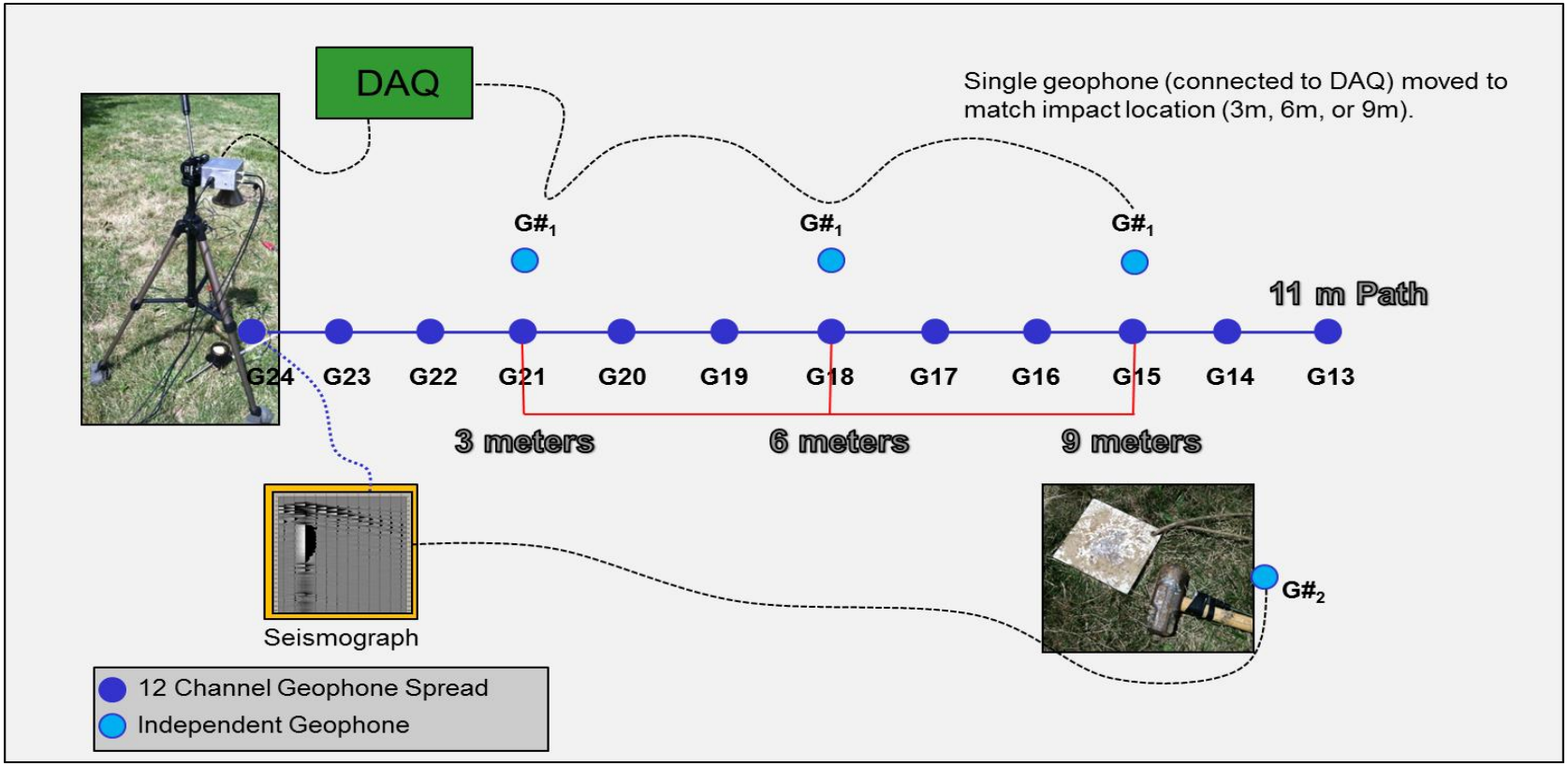

Figure 8. Schematic of outdoor field experiment setup.

The flat, grass-covered path of the experiment was 11 meters long with a spread of 12 single-component (vertical), 4.5 Hz geophones evenly spaced into the ground at one meter apart. The same subsurface path was assumed comprised of homogeneous materials considering the location and small sample area. The 4.5 Hz geophone was selected to allow detection of minute movements with characteristic low frequencies. Deploying these readily available low frequency geophones made it possible to observe the broadest bandwidth of frequencies (i.e. all those greater than 4.5 Hz). The CW 35 GHz radar was mounted at roughly 0.92 meters above the ground on a tripod stand which had foam padding beneath each leg to isolate it from surface vibrations and protect it from introducing internal noise with the received signal. The bell of the radar was pointed nadir at a hand-held retroreflector placed directly beneath it on the earth's surface. The retroreflector was a necessary instrument as it reflected induced vibrations the radar was able to capture. The first geophone (G24, also referred to as the 12^{th} geophone trace) was collocated next to the retroreflector and linked to the seismograph as well as the next geophone (G23). The latter interconnection was important because it allowed the seismograph to record the passage of seismic waves through subsurface soil at each geophone. The seismograph was also connected to an independent geophone attached to the sledge hammer source which served as a time stamp for each trigger. Dr. Hauser repeated each trigger to maintain consistency in magnitude of each induced seismic vibration for all tests performed and ensured each trigger encompassed a single strike. The trigger occurred when the sledge hammer was swung into contact with a small steel plate on the ground. The sledge hammer and steel plate were moved to three different impact distances (3, 6, and 9 meters) from the radar unit where several triggers were

initiated and vibrations recorded at each location for later processing. A single floating geophone connected to the radar DAQ was also moved to each impact location with a sole purpose for recording the time each trigger occurred.

Figure 9. Pictures 1 and 2 provide two different views of the 11-meter experiment path. Picture 2 especially depicts the geophone spread evenly spaced at one meter apart to the right of the measuring tape marking the line of the path. Picture 3 is a close-up of one of the single-component geophones used in the experiment.

Figure 10. Pictures 1 and 2 display the 35 GHz CW radar and tripod set-up with foam padding beneath each leg. Picture 3 is a close-up of the retroreflector used directly below the nadir-pointing radar bell.

Figure 11. Both pictures 1 and 2 display equipment used to induce all seismic activity recorded during the experiment. Picture 1 shows a close-up of the steel plate as well as the floating geophone attached to the radar DAQ and collocated next to a regularly spaced geophone in the spread. The independent geophone attached to the sledge hammer used for time stamping each trigger is also shown in this first picture. In the 2nd picture, Dr. Hauser is captured in action striking the steel plate to trigger a seismic wave during one of the recordings.

SUMMARY

The two-phase research approach described in this chapter was important to capture all parts necessary for comprehensive analyses of results. Setting LEEDR inputs appropriately to consider rain scenarios or specific moisture profiles for cloud scenarios was significant to truly characterize impacts on wavelength performances and especially at 35 GHz. The atmospheric attenuation portion's investigation of how a variety of weather conditions could hinder transmittance at each of the six wavelengths was just as crucial as conducting the actual field experiment as it supported the instrumentation choice in the second part of this study. Therefore, individual steps described to perform both parts of the research approach were vital to promote the foundation of realistic conclusions. Post field experiment investigations on seismic returns as well as per wavelength transmittance results are discussed in full detail in the next chapter.

Chapter IV: Results

General Overview

This chapter provides a synopsis of results for both Parts I and II of the research approach by covering the atmospheric attenuation impacts modeled by LEEDR as well as the received radar and seismograph measurements from the outdoor field experiment. The atmospheric transmission results for each of the six wavelengths are first discussed based on clear, weather-event-free conditions at the 50^{th}, 1^{st}, and 99^{th} RH percentiles. Next, LEEDR-modeled results of expected transmission based on individual inclusion of four different clouds types and six different rain rates are both numerically and graphically demonstrated. Comparative plots made using MATLAB display per weather type transmission results for a bandpass covering the six wavelengths studied. A detailed description of how the radar and seismic assessments are performed using MATLAB is also presented. Lastly, results from the outdoor field experiment as viewed from both the radar and the collocated 12^{th} geophone (G24) from the seismic array are also graphically displayed to better highlight how well the radar detects seismic activity when the impact location changes from 3, 6, and 9 meters away. Chapter V addresses the analyses of results with respect to both the atmospheric transmission and the radar detection of seismic activity.

Results of LEEDR Simulation Scenarios

Part I of this research provides two categories of results for a 1525 meter vertical path at six wavelengths of interest considering the same WPAFB ExPERT Site background atmosphere: 1) LEEDR-modeled path transmission based on weather-free conditions for three different RH percentiles (1^{st}, 50^{th}, and 99^{th}), and 2) LEEDR-modeled path

transmission based on individual inclusion of either a specific cloud type or defined rain rate for the 50th percentile RH. In both categories, and for the purposes of this thesis, transmission results are reported as values between 0 and 1, which are translated as the percentage of energy that passes through the defined atmosphere for the given wavelength. Table 1 below presents recorded model results for the first category.

Wavelength	***50th Percentile RH***	***1st Percentile RH***	***99th Percentile RH***
1.0642 μm	0.887616	0.947887	0.666783
1.557 μm	0.942324	0.973905	0.811947
250 GHz	0.28524	0.652099	0.0741684
95 GHz	0.82689	0.926131	0.686318
35 GHz	0.959986	0.977422	0.932404
10 GHz	0.994562	0.997203	0.990541

Table 1. LBL Path Transmission results – no weather added

Results of the 50th percentile RH are given first since this setting is used in category two simulations and represents average or typical moisture conditions for WPAFB for the summer season and 1500-1800 local time block. Similarly, the 1st and 99th percentile results allow LBL attenuation comparisons to moisture extremes (driest and wettest respectively) for the same season and timeframe. This display of results also verifies the 50th percentile transmissions fall between the two extreme percentile values for each wavelength.

Scenarios created using LEEDR to satisfy category two give LBL results which are displayed in Tables 2 and 3 below. Recall, the purpose of these scenarios is to provide insight on specific wavelength performance through various weather events and highlight their operational limitations. Therefore, these wavelength-dependent results are more directly portrayed numerically with a stoplight color definition to denote Poor (red), Decent (yellow), or Excellent (green) transmission values. Thresholds for stoplight colors

are strictly notional and based on an assumption of acceptable values for operational purposes if the ladar or radar platform is placed at an altitude of 1525 meters.

Wavelength	*Fog* *(0-200m)* *100% RH*	*Stratus Continental* *(500-1000m)* *80% RH*	*Cumulus Continental Clean* *(500-1000m)* *80% RH*	*Cumulus Continental Polluted* *(500-1000m)* *80% RH*
1.0642 µm	0.0764801	6.75817E-17	2.48221E-20	4.74466E-34
1.557 µm	0.089879	2.8951E-17	6.94381E-21	2.20876E-35
250 GHz	0.253002	0.177944	0.182399	0.171551
95 GHz	0.805636	0.697225	0.703642	0.687343
35 GHz	0.955458	0.930801	0.932328	0.928406
10 GHz	0.994102	0.991916	0.992055	0.991695

Table 2. LBL Path Transmittance results considering different cloud types per wavelength at 50th Percentile RH. Surface RH values of 100% and 80% were specified using LEEDR's Ground Level tab to prompt saturated adiabatic lapse rate calculations at lower altitudes from default ExPERT (WPAFB) climatology.

Wavelength	*Drizzle* *(2mm/hr)*	*Very Light Rain* *(2mm/hr)*	*Light Rain* *(5mm/hr)*	*Moderate Rain* *(12.5mm/hr)*	*Heavy Rain* *(25mm/hr)*	*Extreme Rain* *(75mm/hr)*
1.0642 µm	0.269172	0.37558	0.191429	0.0576624	0.012898	1.89466E-4
1.557 µm	0.284343	0.398087	0.20211	0.0606419	0.0135008	1.95821E-4
250 GHz	0.0571495	0.0874913	0.0327177	6.34436E-3	8.50873E-4	3.36754E-6
95 GHz	0.353248	0.353234	0.145871	0.0281421	3.44702E-3	8.88448E-6
35 GHz	0.845573	0.795129	0.584664	0.27726	0.0869569	1.59474E-3
10 GHz	0.989151	0.986128	0.968317	0.912421	0.809151	0.460632

Table 3. LBL Path Transmittance results considering various rain rates per wavelength at 50th Percentile RH. All Rain was modeled to occur through the entire vertical path (surface to 1525 meters).

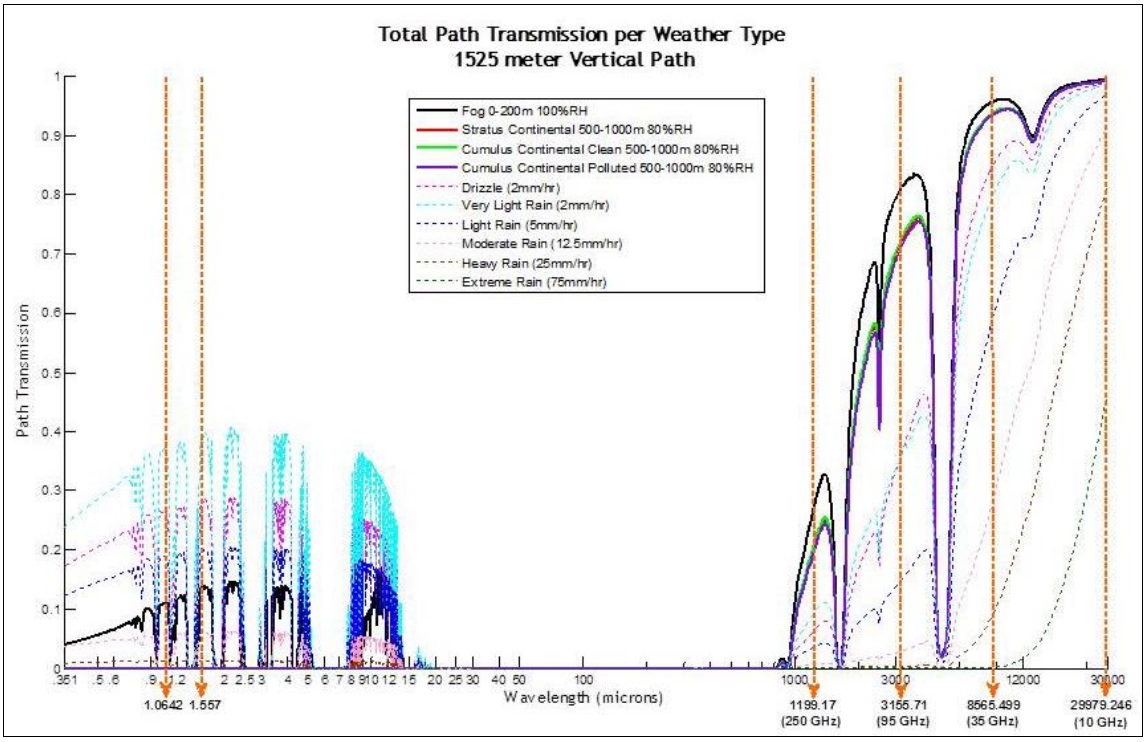

Figure 12. Total transmission impacts from UV to RF for individual cloud and rain type transmission plots along a 1525 meter vertical path through the boundary layer. Plots consider WPAFB ExPERT atmosphere, 50th percentile RH, and GADS aerosols. Again, the six wavelengths studied are highlighted for ease of reference. Note: rain events cover the entire vertical path.

For complimentary visualization purposes, these results are also displayed via total transmission plots per weather event across a wide bandpass (0.351 µm to 10 GHz) covering all six wavelengths studied. These plots were created using LEEDR's Comparisons Tab by running half the spectrum at a time (0.351 – 50 µm Correlated-k and 50 µm- 10GHz LBL) to reduce the computational expense. Results for each transmission plot per weather event, per half of the spectrum are brought together on the composite figure (Figure 12) above. Again, viewing category two's results in full spectrum transmission plots simply presents the big picture of overall impacts on ladar

and radar spectral regimes and quickly identifies which wavelengths are more heavily constrained than others.

Results of Outdoor Field Experiment

To begin analyses on both the seismic array and radar data collections, both datasets are brought into the same program for ease of comparison. MATLAB is a software tool owned by MathWorks that is capable of performing highly technical and computationally expensive analyses by allowing users to uniquely query and manipulate data matrixes via scripts and command line prompts. This same tool also offers visualization options to display data for further interpretation. Therefore, MATLAB is used to read each seismic dataset's .SGY file as well as individual radar test's data housed in a roughly 15 MB .txt file. The two scripts used with the radar and seismic datasets to perform comparative analyses and create figures as described herein are included in Appendix A.

The seismic dataset is investigated first to determine how the 12 geophones (G24-G13) in the array are recorded and interpreted by the seismograph. For the remainder of this document the term 'source' refers to the sledge hammer impact at one of the 3, 6, or 9 meter distances from the radar or 'receiver'. The first figure created while executing the *SeismicDataQuery.m* script shows the entire shot record for the specific test or .SGY file. Running this script for the 5021.SGY and 5024.SGY files where the source was at 3 and 9 meters respectively confirms the seismograph's interpretation of the geophone spread. Since all 12 geophones in the spread are displayed simultaneously, and knowing the associated radar distance from the source, the 12^{th} trace (G24) coincides with the geophone collocated with the radar unit at 0 meters; trace 1 coincides with G13 at the 11^{th}

meter from the receiver. Figure 13 below is the 9 meter representation of the shot record obtained by the seismograph.

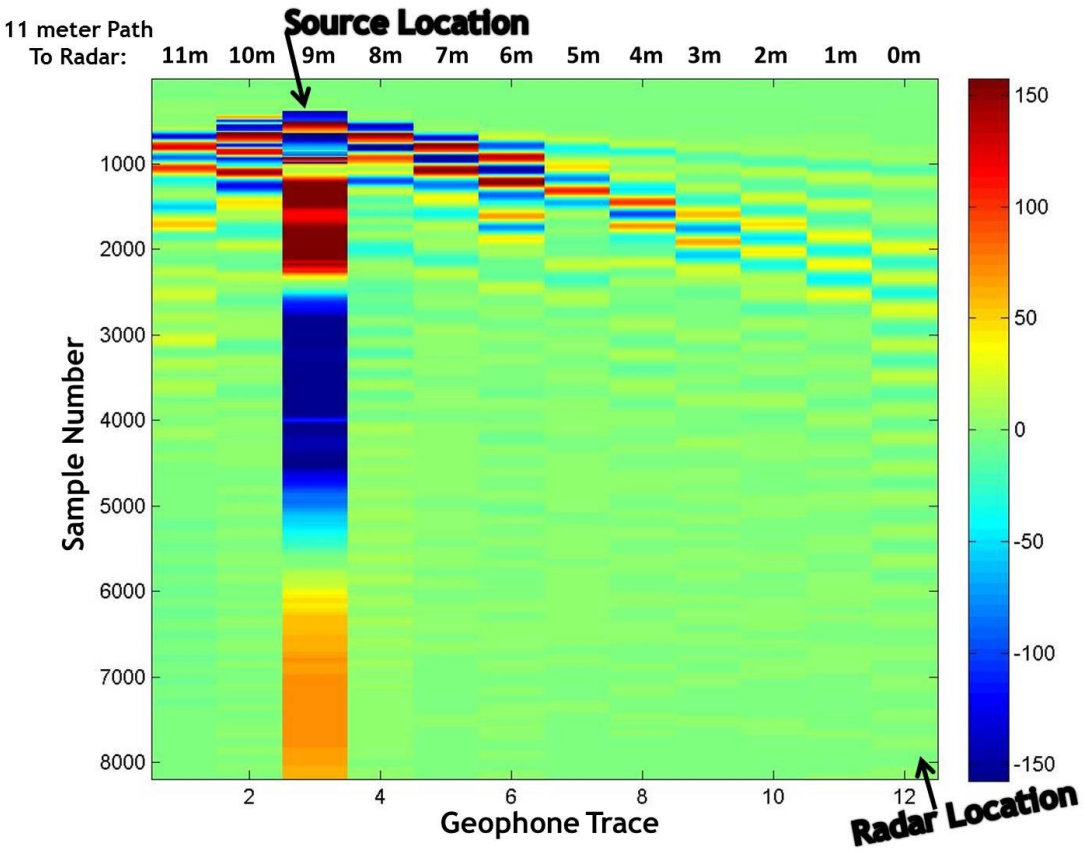

Figure 13. 9 meter shot record output as interpreted by field experiment seismograph. The color bar denotes the voltages recorded by each geophone.

To ensure the seismograph would capture the induced seismic wave traversing the 11 meter path during the field experiment, it was programmed to begin collecting data 10 ms prior to the trigger. The next portion of the *SeismicDataQuery.m* script is used to verify this lead time and determine the new T_0, or the true start of actual seismic data collection, based on a plot of the geophone trace coincident with impact site. To display the associated voltage dataset in terms of time instead of in its raw form of trace voltages versus sample, the .SGY header must be interpreted. Each .SGY header indicates there

are 8,192 samples following a sample interval of 3.1 x 10^{-5} where the first sample begins at the interval value. The script applies this interval to the associated x-axis vector which essentially converts sample number to time in terms of seconds. The script then converts this time vector to milliseconds (ms), which is the common way to display seismic records. The new figure generated at this point can now be studied to determine the time of onset of energy (i.e. the first time the trace begins to show a spike in voltage). In every test considered at 3 (5021.SGY), 6 (5018.SGY), and 9 meters (5024.SGY), the source trace confirms the new T_0 occurs at the end of the programmed 10 ms lead time. To illustrate this approach, Figure 14 is included below.

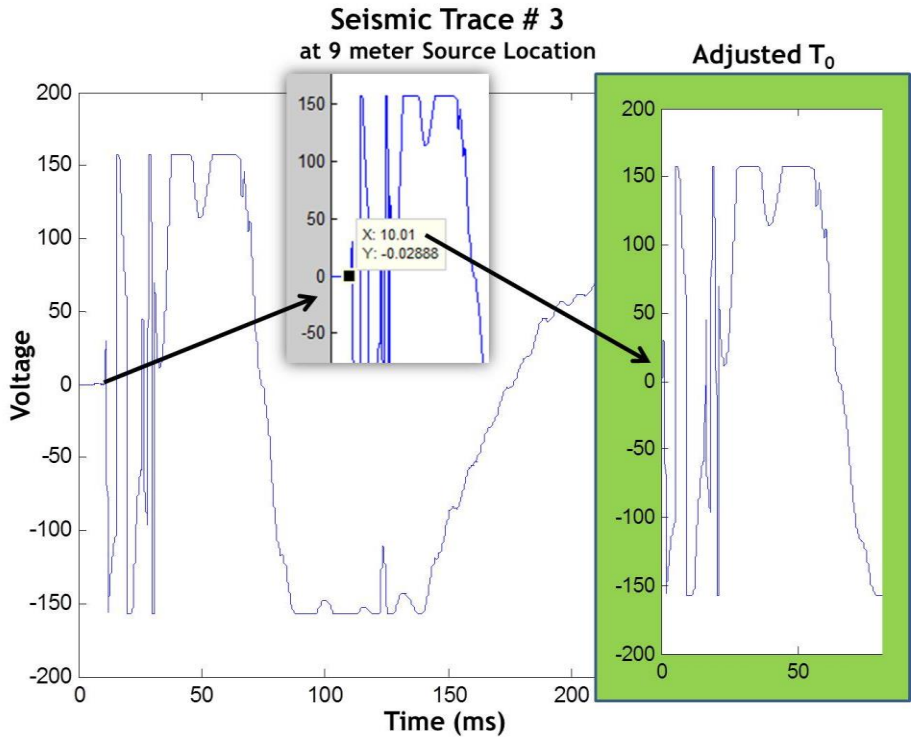

Figure 14. Seismic trace 3 located at 9 meter source location. *LEFT:* Original trace display including the 10 ms pre-trigger data. Used to determine the initial spike in energy begins at 10.01ms. *RIGHT:* Resulting trace 3 plot with adjusted T_0 = 0 ms.

The next portion of the *SeismicDataQuery.m* script applies a 10 ms shift to trace data adjusting T_0 (time of impact) to 0 ms as shown for proof of concept on the right side of Figure 14 above. This is an important adjustment as every trace in the spread began collecting data 10 ms prior to the induced seismic wave. Therefore, removing associated undesirable data in the 12^{th} seismic trace beneath the receiver for the .SGY of interest promotes ease of interpretation when later compared to radar test data of the same source distance and ensures the start of trace occurs at 0 ms. The new figure created of the 12^{th} seismic trace at this point in the script is retained for further scrutiny after the accompanying radar data is plotted.

A switch to the *RadarDataQuery.m* script is now required to first execute the portion of code that pulls only the radar DAQ geophone's data from a radar test with the same distance to source as just queried in the *SeismicDataQuery.m* script (i.e. Copy of test18.txt, Copy of test15.txt, and Copy of test21.txt for 3, 6, and 9 meter locations respectively). As mentioned in the Methodology chapter, the floating geophone connected to the DAQ was moved to be co-positioned with the impact location to serve as a time stamp for the radar data collection. Therefore, since the radar was CW, this time stamp is necessary to determine T_0 much like for the seismic data. To plot the DAQ geophone versus time in milliseconds, the radar Copy of Test#.txt file header is reviewed to identify the number of samples (500,000) per test and the sample interval (10 μsec) that's invariable in all collected radar datasets. To run the *RadarDataQuery.m* script, the original Copy of Test#.txt file should be stripped of the header leaving only the geophone, I and Q phase data columns before resaving as a Copy of Test#_NoHeader.txt

file. The latter simply makes querying the dataset less cumbersome by avoiding the need for specific code to work around the header text. Note, due to uncertainty in which column represented the I or Q data for the two radar columns, the remainder of this thesis will reference them as r and r2. Once the script applies the interval to the samples, this x-axis data is then converted from time in seconds to milliseconds. The script can now be executed to plot the DAQ geophone data against time in milliseconds. As described for the seismic trace T_0 adjustment, the initial time the trace begins to show a spike in energy is identified, and a T_0 shift is applied to all data in the radar dataset (r, r2, and DAQ geophone) for the test considered. It is important to note the time to apply in the shift is not the same value for each impact location's test. The radar data collection (r, r2, and time synchronization (DAQ) geophone) was manually started immediately preceding the strike. Total data collection time was 5 seconds. Therefore, this T_0 shift identification is re-accomplished per radar dataset.

Lastly, the second execution of a separate portion of the *RadarDataQuery.m* script code applies a smoothing technique (serving as a low pass filter) to filter the high frequency noise accompanying a 100 kHz data acquisition rate so the overall shape of the seismic energy signal is more visible. The suggestion to use a moving average window on the r and r2 data came from a discussion with subject matter experts, Dr. Fiorino, Dr. McCrae, and Dr. Basu with the AFIT/CDE. Further discussion with radar expert and AFIT PhD candidate, Lee Burchett, determined the MATLAB convolution command to be the most efficient smoothing technique considering the type of dataset and comparative purposes. As commented in the *RadarDataQuery.m* script, a 50 point

moving average window (i.e. low pass filter) is hard coded for both the r and r2 vectors. In some instances, for clearness of display, the r data is scaled as necessary to better compare with seismic data. The final figure generated by this section of the script is left open for additional seismic data to be overlaid next.

Returning to the last figure created and retained of the 12th seismic trace considering the T_0 shift, the difference in voltage amplitude is significantly greater (by about 2 orders of magnitude) than that observed in the final r and r2 radar figure. Therefore, for clarity purposes, the seismic trace is scaled down to the radar returns. Executing this portion of the *SeismicDataQuery.m* generates a new plot reflecting the scaled output. This resulting 12th geophone trace is overlaid on the open radar figure made during the second execution of the *RadarDataQuery.m* script to create a single comparative figure for analyses.

In the final sections of both *SeismicDataQuery.m* and *RadarDataQuery.m* scripts a Fast Fourier Transform (FFT) calculation is executed on the 12th seismic trace and the radar (r) data. Note, the basic FFT algorithm inherently considers all data points available. Performing an FFT on each dataset independently presents results in a new perspective where peak frequencies in each can be directly compared to determine if the two instruments observed the same induced seismic activity.

The full process described above is repeated for each of the source distances at 3, 6, and 9 meters. However, only results from the source located at the farthest test distance of 9 meters are discussed. Figures 15 – 17 below show the final results from executing both the seismic script (interrogating the 5024.SGY file) and radar script (interrogating

the corresponding Copy of test21.txt file) in their entirety. Figure 15 displays both radar (r and r2) returns compared to seismic trace #12. This wide view of the time series exemplifies the need to truncate the extra data collected beyond the timeframe the vibration passed the radar unit. Thus, remaining comparative figures only display the portion of time series the seismic trace collection occurred. Recall an FFT algorithm will consider all data which, in this instance, includes the radar returns past the geophone and where the r and trace #12 signals are not comparing well. During the radar script run the truncation code targets the range in time where r data is believed to demonstrate seeing the seismic vibration. Therefore, truncation greatly benefits the FFT calculations made by removing the extra 'noise' concealing the true returned signal of interest. The decision to omit r2 plots from further comparisons comes from reviewing several tests which suggest the return is not consistently strong enough for consideration in these analyses. This is not surprising or unexpected since for very small amplitude vibrations (<< wavelength of ~ 1 cm), either the I or Q channel could be near a null point in sensing.

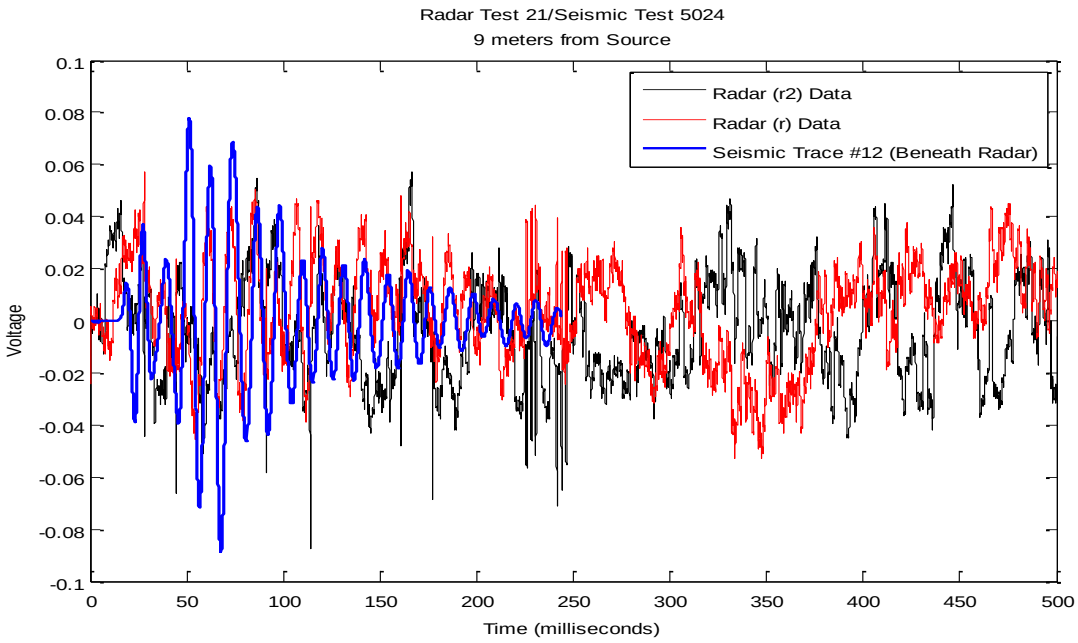

Figure 15. *Wide View* - Final radar and collocated seismic trace comparison with source at 9 meters.

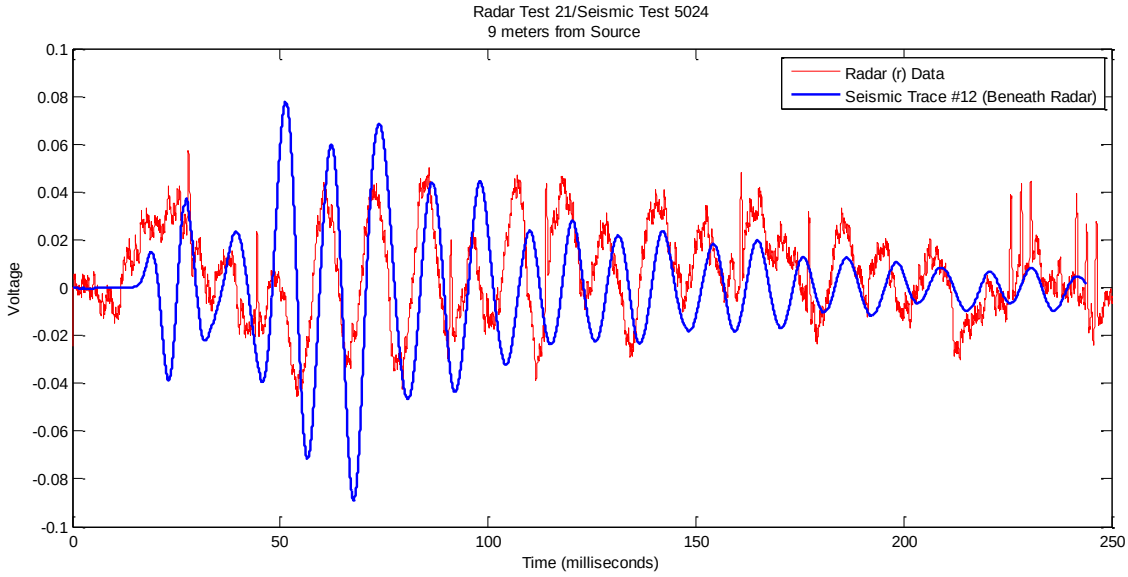

Figure 16. *Zoomed-in View* - Final radar and collocated seismic trace comparison with source at 9 meters.

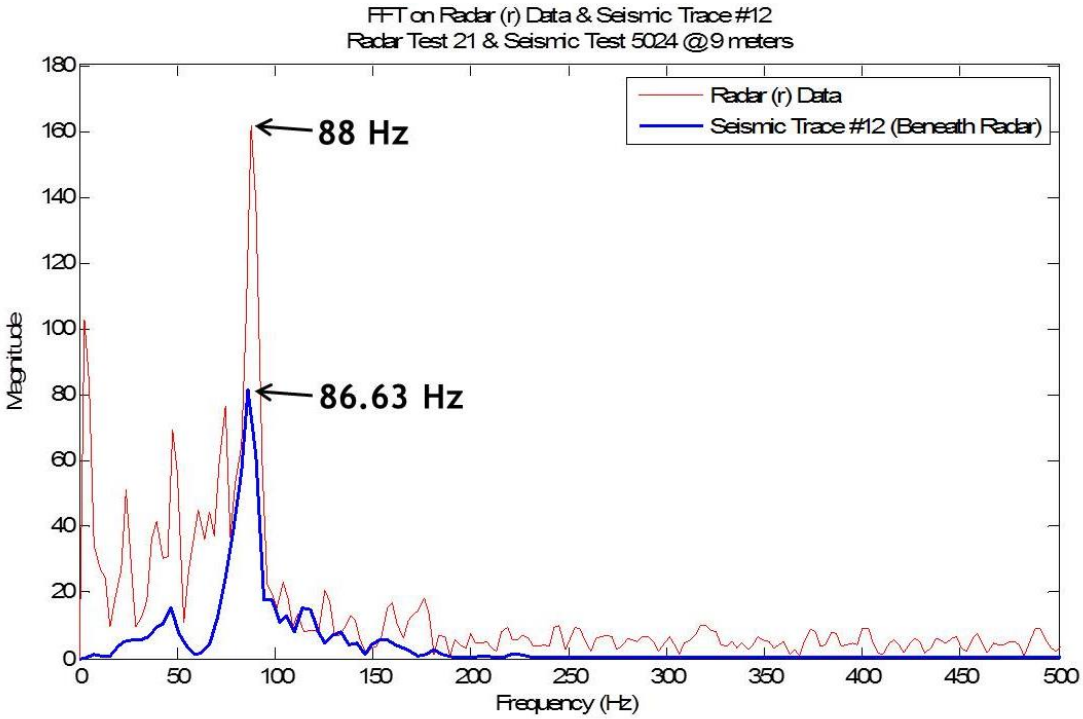

Figure 17. FFT comparison results from radar (r) data and collocated seismic trace #12 with source located at 9 meters.

INVESTIGATIVE QUESTIONS ANSWERED

Results given above resolve one main question in each component of this two-part research project. First, the optimal wavelengths with widest flexibility of operation among weather conditions can be ascertained from transmission tables. Second, and perhaps in answer of the ultimate research goal, seismic and radar comparison plots confirm that a 35 GHz radar is capable of observing induced seismic vibrations, and the source distance it can provide the clearest returns. Peripheral conclusions based on these two main solutions can also be made; all of which are summarized in the next chapter.

Chapter V: Conclusions/Future Research

General Overview

Based on the results presented in the previous chapter, analyses on the outcome of novel approaches performed are conclusively brought together in this chapter. The final section of this chapter acknowledges areas where additional or extended research could be completed to further solidify these initial findings.

Conclusions of LEEDR Simulation Scenarios

The 50th, 1st, and 99th RH percentile comparison results shown in Table 1 give the first confirmation that the effects of water vapor absorption are a maximum at 250 GHz. Water vapor absorption effects are also notable at 95 GHz at the most moist percentile (99th). Another effect evident in Table 1 is the RH impact on aerosol size which is seen at the 99th percentile for the 1.0642 μm line. In each of the three percentile cases studied for the six wavelengths, 250 GHz gives the least amount of transmission. Under average or typical clear atmospheric conditions for WPAFB during the summer season between 1500-1800 local, each of the remaining five wavelengths perform excellently according to notional threshold definitions where Poor (red) ranges from 0-49%, Decent (yellow) ranges from 50-75%, and Excellent (green) ranges from 76-100% transmission. One further observation from this table is the consistently high transmission results above 90% for both 35 GHz and 10 GHz in all moisture extremes.

As weather conditions are individually added to the background WPAFB ExPERT atmosphere defined, the operational flexibility of each wavelength is better assessed. Tables 2 and 3 explicitly highlight performance strengths and weaknesses numerically

while Figure 12 further demonstrates these same distinctions across the wide spectral band of the 6 wavelengths. Instantly, it becomes clear the microwave regime (with the exception of 250 GHz) largely outperforms all other shorter wavelengths when clouds or rain are introduced into the vertical atmospheric profile. Cloud droplet sizes can vary from about 5-50 μm, drizzle is roughly ~100 μm (0.1mm) in size, and rain drops are on the order of ~0.1-3 mm *(Petty, 2006)*. In these instances, 1.0642 μm and 1.557 μm are dominated by Mie scattering and are thus significantly degraded in terms of transmission. It is interesting to note in comparison to 250 GHz, that although the latter is only slightly less impacted by clouds, it still takes a bigger hit than even the visible and ladar wavelengths in rain conditions. Again, this proves effects of the maximum extinction efficiency occurring at 250 GHz is due to its size being nearly the same or larger than the rain particulates. As both Tables 2 and 3 and Figure 12 describe, 95 GHz sits solidly in the Rayleigh scattering regime for clouds, but transmission is hardly impacted due to the λ^{-4} intensity rule. Therefore, results shown agree with theory that 95 GHz performs well (excellent) under foggy conditions and fairly well (decent) through the low level cloud types. However, its performance during any type of rain event degrades transmission too strongly for operational consideration as its scattering regime transitions to Mie. The final two microwave frequencies studied prove to be the most ideal for operational use during weather events. Either the 35 GHz or 10 GHz will sufficiently see through low level clouds. The main separation occurs when any rain event stronger than light rain comes into the scenario; before the moderate rain rate is encountered, 35 GHz meets an excellent threshold for drizzle and very light rain and is still considered decent for achieving greater than 50% transmission results in light rain. Ultimately, the wavelength

with the greatest flexibility for successful operation under the most types of weather studied is 10 GHz. At 10 GHz (3 cm), and in the exception of extreme rain rates, rain proves to be less of an attenuator since the wavelength is much larger than the drop sizes. Perhaps more importantly, this wavelength is capable of seeing through low level clouds.

When making final conclusions between 35 GHz and 10 GHz as the optimal wavelength to satisfy Part I's research objective, the typical size of these instruments must be considered. A 10 GHz radar is more cumbersome compared to the portable, hand-held size of the 35 GHz system because to obtain the same diffraction limited spatial resolution, an antenna 3.5 times larger than the 35 GHz would be required (per λ/D). The diffraction limited resolution of the 35 GHz module is desirable due to the higher sensitivity to vibrations or displacements (as governed by $disp./\lambda$) of the ground that are anticipated to exist. Therefore, if the mission were to more covertly monitor underground activity, the 35 GHz radar is the instrument of choice and its use in completing Part II's measurements is further supported. In summary, another advantage of the shorter wavelength system is its higher frequency with increased phase shift in response to seismic returns. Even if the same displacement occurs between a 35 GHz and 10 GHz system monitoring the same event, the longer wavelength (lower frequency) will have a decreased phase shift. *(Petkie et al., 2008).*

Lastly, before moving to a discussion on the conclusions of Part II, it is appropriate to further point out how well the results of Part I matched with similar world-wide vertical profiles assessed in *Fiorino et al. (2010).* Two types of paths were reviewed in the 2010 study, and this suggests that wavelengths may perform differently in more

horizontal or slant path scenarios due to how the paths change the amount of atmosphere traversed. With the exception of performance at 1.557 μm, results of this thesis are in alignment with vertical profile conclusions made for the same three wavelength comparisons considered (1.557 μm, 250 GHz, and 95 GHz). However, some disagreement on the success of a 1.557 μm ladar's ability to penetrate through fog can be attributed to the *Fiorino et al.* (2010) study using signal-to-noise ratio as the comparison metric rather than transmission.

Conclusions of Outdoor Field Experiment

Part II of this research revolves around one main question: can a 35 GHz CW radar see induced seismic vibrations when pointed directly nadir at a retroreflector on the earth's surface? Peripheral questions spun off from here, pondering the maximum distance from the source that could supply a sufficient return and the general seismic wave type which could be observed if the experiment were successful. Results shown in Chapter IV can assuredly verify conclusions made through the remainder of this chapter in response to these questions.

Although not the main scope of this research, and while acknowledging there may be other wave types possibly detectable through analyses of the entire shot record, some speculation on the waves observed during the experiment can be hypothesized. Figure 5.1 (A) found in the fifth chapter of *Reynolds, 2011* (page 180) depicts the basic phases of a wave and how they typically travel. Direct waves (a type of P-wave) travel more horizontal with propagation, but a critically refracted P-wave generates a head wave which causes vertical particle motion with respect to the geophone sensors. Thus, it is

sensible to state there was possible shallow P-wave (body wave) refraction present in the underlying path contributing to the vertical motion detected by the sensors at the surface. The accompanying example seismic refraction record, (B) of the same Figure 5.1, shows how analyzing the compilation of individual geophone traces along a path can provide a deeper understanding of the event. This lower schematic places the shot point location in the upper right corner. Each trace is representative of a geophone's recording with increasing offset to the left. The first wave arrivals per trace highlight that direct waves generally cause a weaker geophone response, but refracted waves become more apparent. Additionally, the large amplitude or stronger surface waves are very prominent due to the vertical component of Rayleigh waves. These conclusions could have been reasonably predicted given the single component geophones used in the experiment inherently have vertically positioned coils making them sensitive to movement in the same direction. Figure 5.1 (B) also confirms an increased offset typically provides clearer returns due to waves becoming more established and separated with time. The latter statement further supports that results of the larger 9 meter offset were logical for the focus of analyses in this study. *(Reynolds, 2011; Hauser, 2015).*

As results suggest in Chapter IV, the 9 meter source location provided the clearest returns allowing true determination of whether the radar was capable of seeing the induced seismic vibration. Most importantly, from comparative FFT results on both the collocated seismic trace (#12) and the radar (r) data, it is conclusive the radar can detect such a seismic event. Figure 17 shows the dominant frequency in the r data to be at 88 Hz; basically the same core signal observed in trace #12 at 86.63 Hz. The fact that both

detection instruments share the same peak frequency in their FFT results is sufficient to make such a definitive statement. Another interesting discovery, although lower in magnitude, is the utility frequency (~60 Hz) that the radar captured. This proves the methodology used could also see common environmental signals like those suggested in the 2010 Sandia project *(Senglaub et al., 2010).*

Recommendations for Future Research

From an experiment methodology perspective, a few alterations could be made to further study or enhance research completed within the bounds of this thesis. Small details such as changes in the way the radar could be stabilized to decrease the introduction of jitter could make received radar signals easier to discern. In future research, a geophone could be placed on a cart along with the radar as a way to track the amount of internal movement or noise coming from the cart's response to the ground vibrating. If this data were recognized it could be removed from the final analyses. This could become especially important if the radar were placed on an airborne, moving platform where compensation for extra motion would undoubtedly be required. On a similar note, the metal retroreflector could have a vibration it resonates as a result of the induced seismic impact. To account for this, the retroreflector could be anchored to the ground with stakes. Future work using 3-component geophones instead of vertical component geophones to examine what other wave forms may be present could more completely document all wave phases of the seismic energy.

As an expansion to this thesis and assuming these vibrations are detectable enough, secondary tests to determine if induced vibrations in tunnels below WSU campus can be

sensed at the earth's surface could significantly contribute to results. Additionally, since the radar used to obtain results is an active sensor, this could hinder interest in military applications. Experiments using a passive sensor could uncover promising results for missions which may require a degree of covertness. Another research angle could be to extend the path over which the signal is transmitted to an airborne or space-borne platform carrying a receiver such as a Synthetic Aperture Radar (SAR). Doing so could prompt results with achieved greater resolution while operating at more standoff distances. The latter study could then also use LEEDR by including numerical weather forecasts instead of probabilistic climatological profiles used in Part I. Lastly, an incentive for quantifying rain impacts could justify the need to perform similar field experiments during actual rain events. Knowing that radars are uniquely sensitive to rain, if the ability to quantify ground vibrations from rain were incorporated, then this 'weather noise' could be removed from radar returns in such a way that only vibrations from the true geological activity could be pronounced. This extended research could eliminate restrictions on the same proposed method of seismic detection described throughout this thesis.

Each of these recommendations mentioned for future work would capitalize on the single most important goal of this thesis: to realize new ways of monitoring otherwise invisible illegal or terrorist-like activities for the security of this nation. When researchers come together to meet a common goal, the possibilities are endless.

Appendix A

RADARDATAQUERY.M

```
% You must first delete the header from the original .txt file and save
as a new '_NoHeader.txt' for each test prior to running this code!

% Original header states there are 500,000 Samples per test with a
sample interval of 1.0E-5.
% FOR REFERENCE:
% Test18 = 3 meter test
% Test15 = 6 meter test
% Test21 = 9 meter test

M=dlmread('Copy of test21_NoHeader.txt','\t');
MyData(:,1) = linspace(0,5,500000)'; % prime sign converts the row to a
column
M(:,1) = MyData;   % Need this to pull out & call x-axis/Time vector
specifically/separately
ConvertToMilliSec = 1000;
M(:,1) = MyData .*ConvertToMilliSec;
%M2 = M(find(M(:,1) > 2044 & M(:,1) < 2044.01):end,:); %T0 adjustment
from Radar DAQ geophone at 6 meters
%M2 = M(find(M(:,1) > 505.2 & M(:,1) < 505.21):end,:); %%T0 (Test
18)adjustment from Radar DAQ geophone at 3 meters
% M2 = M(find(M(:,1) > 587.2 & M(:,1) < 587.21):end,:); %%T0 (Test
20)adjustment from Radar DAQ geophone at 3 meters
M2 = M(find(M(:,1) > 1132 & M(:,1) < 1133):end,:); % %T0 adjustment
from Radar DAQ geophone at 9 meters.
% Must edit this line per Test to find each new T_0. Will COMMENT OUT
lines 15-26 1st script run.
x = M2(:,1) - 1132;    % Update per test (505.2, 1135, 1132 for 3,6,9
meters respectively).
c= conv(M2(:,3),ones(50,1)./50,'same');   % 3(test18) & 9 Meter Tests.
Smoothing with 50 pt window; ./50 Normalizes; 'same' = retains size of
M2(:,3) vector.
r=c-.05; %scaling for clarity
r2 = conv(M2(:,2),ones(50,1)./50,'same'); % 3(test18) & 9 Meter Tests.
%r   =   conv(M2(:,3),ones(50,1)./50,'same').*(-1);     %   6   (and   3-
Test20)Meter Tests.
%r2   =   conv(M2(:,2),ones(50,1)./50,'same').*(-1);     %   6   (and   3-
Test20)Meter Tests.
%r = M2(:,3);    %The Q data? Only use 2nd script run to view radar w/o
smoothing
%r2 = M2(:,2);  % The I data? Only use 2nd script run to view radar w/o
smoothing
```

```
%g = M2(:,4);    % Radar DAQ geophone
%x = M(:,1); % COMMENT OUT - 2nd run. Used to view original (pre-T0
adjusted)geophone data.
%g = M(:,4);     % COMMENT OUT - 2nd run. Radar DAQ geophone. Used to
view original (pre-T0 adjusted)geophone data.
% figure();
% plot(x,r,'red')    % COMMENT OUT - 1st script run
% %hold on
% %plot(x,g,'blue')  % COMMENT OUT - 2nd script run
% hold on
% plot(x,r2,'black')  % COMMENT OUT - 1st script run
% title('Radar Test 21 @ 9 meters (Seismic Test 5024)');   % Need to
update per Test!
% xlabel('Time (milliseconds)');
% ylabel('Voltage');

%% ATTEMPT FFT -
r=r(5000:22500); %apply a range to perform the FFT on so no noise is
considered
r = [r;0;zeros(20000,1)]; %needed to pad the end so the vectors are the
same length
Fs = 1/1e-5; %sampling frequency (in samples per second)
if mod(size(r,1),2) == 0 %if even number of points
    NFFT = size(r,1); % NFFT = number of points in the input to the FFT
else
    NFFT = size(r,1) + 1; % if odd number of points
    %r = [r;0;zeros(20000,1)];  %switch to r2 as necessary
end
X = Fs/2.*linspace(0,1,NFFT/2+1); % this defines the first half of the
x-axis (x values)for first half of r data
r=r-mean(r); % takes care of any DC offset...removes noise
Y = fft(r); % Fast Fourier Transform on radar data in column 3.
Y = Y(1:NFFT/2+1); % grabs the first half of data we care about
figure('name', 'FFT Radar (r) data - Test 21 @ 9 meters');
plot(X, abs(Y)); % take the absolute value to include magnitudes of
imaginary values too
title('FFT on Radar (r) Data - Test 21 @ 9 meters');  % Need to update
per Test!
xlabel('Frequency (Hz)');
ylabel('Magnitude');
```

SeismicDataQuery.m

```
% The first set of code calls the whole shot figure - it's useful to
verify the source distance for the .SGY file.
% Note - you will need to switch out the .SGY file name per interest.
The SGY Header states the time/sample interval is 3.1000E-5 and there
are 8,192 samples.
% FOR REFERENCE:
% 5021.SGY = 3 meter test; Trace #9 @ Source/impact location
% 5018.SGY = 6 meter test; Trace #6 @ Source/impact location
% 5024.SGY = 9 meter test; Trace #3 @ Source/impact location

[Data,SegyTraceHeaders,SegyHeader]=ReadSegy('Y:\CDE        Staff\Via\Via
Thesis 2015\Radar Seismic Quad 1\SGY\5024.SGY');
h = figure(); imagesc(Data);colorbar    % Makes an image of the raw
seismic array.

% The following code pulls the specific trace out and plots only that
trace #'s data in terms of either seconds or ms. Note - you will need
to switch out the .SGY file name per interest AND the specific trace of
interest!

%The Trace # below will need updated from the impact location trace to
the trace beneath radar (#12 always).
[Data,SegyTraceHeaders,SegyHeader]=ReadSegy('Y:\CDE        Staff\Via\Via
Thesis 2015\Radar Seismic Quad 1\SGY\5024.SGY', 'traces', [12]);
%%%figure();plot(Data);     % Uncommenting = Just a reference point for
original display
Timeline =linspace(3.1000e-5,.253952,8192)'   % Takes into account the
time/sample interval given in the .SGY header (3.1000e-5). It doesn't
start at time ZERO, but rather at the interval value. The ' (or prime)
notation switches vector from a row to a column.
%%%figure();plot(Timeline, Data);     % Uncommenting = Shows the correct
x-axis in terms of time in SECONDS

ConvertToMilliSec = 1000;
NewTimeline = Timeline .*ConvertToMilliSec;
figure();plot(NewTimeline,Data);   %   Shows   the   data   in   terms   of
milliseconds

T2=NewTimeline(find(NewTimeline==10.013000000000000):end)-10.013; % Use
this to account for the adjusted T_0 at impact location
figure();plot(T2,   Data(find(NewTimeline==10.013000000000000):end))   %
Final trace figure in terms of milliseconds.

NewData = Data./400; % Use to scale down based on 10 ms (T2) lead-in
only
%%figure();plot(T2,NewData(find(NewTimeline==10.013000000000000):end));
% Shows scaled down trace

% ATTEMPT FFT
Fs = 1/3.1e-5;
```

```
if mod(size(NewData,1),2) == 0 %if even number of points
    NFFT = size(NewData,1); % NFFT = number of points in the input to
the FFT
else
    NFFT = size(NewData,1) + 1; % if odd number of points
    NewData = [NewData,0];
end
X = Fs/2.*linspace(0,1,NFFT/2+1); % this defines the first half of the
x-axis for first half of geo data
NewData=NewData-mean(NewData); % takes care of DC offset..
Y = fft(NewData); % Fast Fourier Transform on Trace #12 data
Y = Y(1:NFFT/2+1); % grabs the first half of data we care about
figure('name', 'FFT of Seismic Trace #12 - Test 5024 @ 9 meters'); % to
include intensities of imaginary values too
plot(X, abs(Y)); % take the absolute value to include magnitudes of
imaginary values too
title('FFT on Seismic Trace #12 - Test 5024 @ 9 meters');  % Need to
update per Test!
xlabel('Frequency (Hz)');
ylabel('Magnitude');
```

Appendix B

Ducommun

Doppler Sensor Heads

Bulletin No. SRF

FEATURES

- High sensitivity
- Low 1/f noise
- Circular polarized waveform
- Low harmonic and spurious emission
- Temperature and vibration qualified
- Compact size
- Low cost and volume production

APPLICATIONS

- Automotive Radar
- Doppler Radar
- Directional sensor
- Long range motion detector

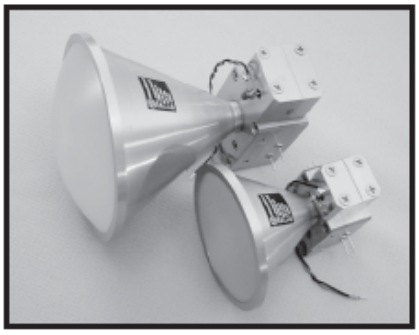

SRF Series

DESCRIPTION

SRF series Single and Dual Channel Doppler Sensor Heads are designed for **long range** motion/speed/directional detection where the sensitivity is essential. The sensors are constructed with a high performance horn antenna or horn-lens antenna, a linear to circular polarizer and T/R diplexer, a balanced mixer (I/Q mixer for dual channel version) and a high performance Gunn diode oscillator or dielectric resonator oscillator/multiplier chain. The low 1/f noise mixer diodes and high performance oscillator enhance Doppler detection at low IF frequency and circular polarization waveform improves reception ability for various Radar targets. The sensors are offered with single or dual channel version. The dual channel version provides target moving direction (approaching or receding) information of the target while detecting speed.

8

Standard products are offered at 24.15 GHz, 35 GHz and 76.5 GHz, while other frequency bands are available upon request.

SPECIFICATIONS

Typical Specifications (Single Channel)			
Parameters / Model #	SRF-24120610-01	SRF-35120610-01	SRF-77120910-01
RF frequency	24.150 GHz	35.500 GHz	76.500 GHz
Transmitter output power	+10 dBm (typical)	+10 dBm (typical)	+10 dBm (typical)
Receiver conversion loss	6 dB (typical)	6 dB (typical)	9 dB (typical)
IF bandwidth	DC to 100 MHz (minimum)	DC to 100 MHz (minimum)	DC to 100 MHz (minimum)
Antenna 3 dB beamwidth	12 degrees (typical)	12 degrees (typical)	12 degrees (typical)
Antenna side lob level	-20 dB (maximum)	-20 dB (maximum)	-20 dB (maximum)
Polarization	right hand circular	right hand circular	right hand circular
Spurious and harmonics	-16 dBc (maximum)	-16 dBc (maximum)	-16 dBc (maximum)
ΔF/ΔT	-0.20 MHz/°C (maximum)	-0.40 MHz/°C (maximum)	-4.0 MHz/°C (typical)
ΔP/ΔT	-0.03 dB/°C (maximum)	-0.04 dB/°C (maximum)	-0.04 dB/°C (typical)
DC bias	+5.5 V / 250 mA (typical)	+5.5 V / 350 mA (typical)	+5.5 V / 650 mA (typical)
Operation temperature	-40 to +85 °C	-40 to +85 °C	-40 to +85 °C
Outline drawing	WT-C-A1	WT-C-A2	Consult factory

Typical Specifications (Dual Channel)			
Parameters / Model #	**SRF-24120910-D1**	**SRF-35121010-D1**	**SRF-77121210-D1**
RF frequency	24.150 GHz	35.500 GHz	76.500 GHz
Transmitter output power	+10 dBm (typical)	+10 dBm (typical)	+10 dBm (typical)
Receiver conversion loss	9 dB (typical)	10 dB (typical)	12 dB (typical)
IF bandwidth	DC to 100 MHz (minimum)	DC to 100 MHz (minimum)	DC to 100 MHz (minimum)
I/Q Channel Phase	90 °± 10 °	90 °± 10 °	90 °± 20 °
Antenna 3 dB beamwidth	12 degrees (typical)	12 degrees (typical)	12 degrees (typical)
Antenna side lob level	-20 dB (maximum)	-20 dB (maximum)	-20 dB (typical)
Polarization	right hand circular	right hand circular	right hand circular
Spurious and harmonics	-16 dBc (maximum)	-16 dBc (maximum)	-16 dBc (maximum)
ΔF/ΔT	-0.20 MHz/°C (maximum)	-0.40 MHz/°C (maximum)	-4.0 MHz/°C (typical)
ΔP/ΔT	-0.03 dB/°C (maximum)	-0.04 dB/°C (maximum)	-0.04 dB/°C (typical)
DC bias	+5.5 V / 250 mA (typical)	+5.5 V / 350 mA (typical)	+5.5 V / 650 mA (typical)
Operation temperature	-40 to +85 °C	-40 to +85 °C	-40 to +85 °C
Outline drawing	WT-C-A1	WT-C-A2	Consult factory

OUTLINES

WT-C-A1

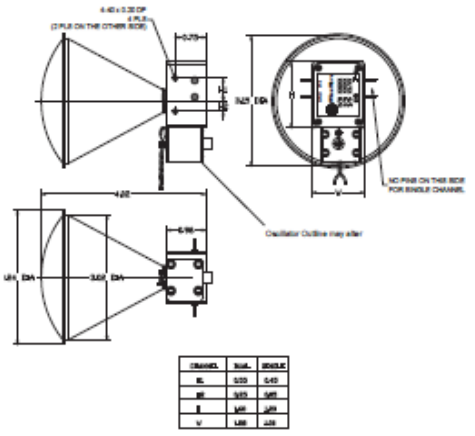

K Band Doppler Sensor Heads

WT-C-A2

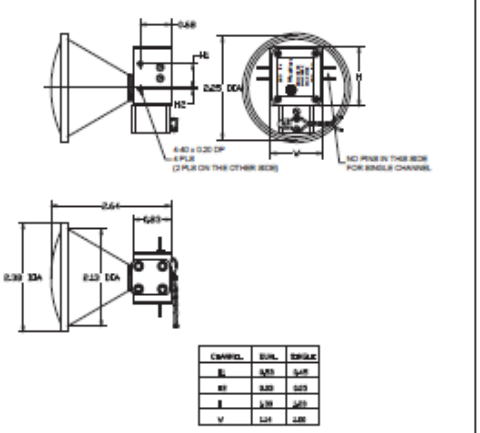

Ka Band Doppler Sensor Heads

Ducommun offers three types of microwave and millimeterwave sensor heads. They are **Doppler Sensor Heads**, **Directional Doppler Sensor Heads (SRF Series)** and **Ranging Sensor Heads (SRR Series)**. The main objectives of the application notes are to explain the basic principles of Doppler Radar and Ranging (Distance) Radar and how Ducommun's sensor heads should be implemented to configure such Radar systems.

Doppler Radar

It is well known that **Doppler Radar** is widely used for speed measurement. The principle behind the Doppler Radar is the frequency shift of a microwave signal bounced back by a moving object. The resultant frequency shift is known as **Doppler Frequency Shift**, which is given by the following equation

$$F_d = 2V (Fo/C) \cos (\theta)$$

Where:

Fo is the transmitter frequency (Hertz).
C is the speed of light, which is 3×10^8 (meter/sec).
V is the speed of the target (meter/sec).
θ is the angle between the radar beam and the moving target (in degrees) as shown in Fig. 1.

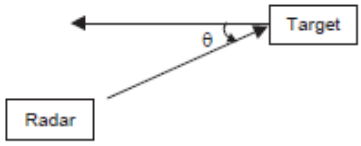

Figure 1. Doppler Shift

When moving target moves perpendicular to the radar beam, the Fd equals 0, which indicates no Doppler shift. On the other hand, the F_d is equal to 2V(Fo/C) when the target moves parallel to the radar beam or if **q** is real small (0 to 10 degrees).

SRF series single channel Doppler sensor heads offered by Ducommun are designed for **long range** Doppler Radar application where detection sensitivity is essential.

The simplified block diagram of a Doppler Radar formed by using Ducommun's single channel sensor head is shown in Fig. 2. A high quality DC power supply for Gunn oscillator bias, a low noise IF amplifier and DSP circuitry are the minimum requirements for a system designer to realize such a radar system. In addition, the moving target radar cross section, detection distance and target speed are the main factors in consideration when specifying the transmitting power, antenna gain and IF frequency bandwidth of the sensor head. The example of the IF frequency range of a 24.15 GHz and 76.5 GHz Doppler radar at various speeds is shown in the following table.

Transmitting Freq. (GHz)	24.15		
Speed (Km/Hr.)	10	80	200
IF (Hz)	224	1,790	4,475
Transmitting Freq. (GHz)	76.50		
Speed (Km/Hr.)	10	80	200
IF (Hz)	709	5,670	14,176

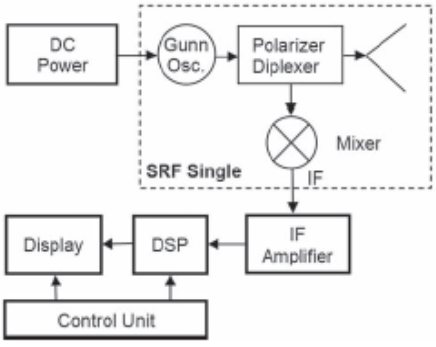

Figure 2. Simplied Doppler Radar

Doppler Directional Radar

In certain applications, one not only has to know the target speed, but also the target moving directions, i.e., whether the target is approaching to the radar or receding from the Radar. The examples for such applications are the law enforcement radar systems used by police officer or door openers in the building entrance. Also, such radar systems are often used for distinguishing vibrating targets, fan rotations or curtain movements caused by the wind from a real intrusion in the security system.

The implement of the directional information is realized by adding an additional mixer to the single channel sensor head with a 90 degrees phase difference. The mixer used in the directional sensor is sometimes known as phase detector or I/Q mixer. The phase relationship between two mixers is that the first mixer will lead the second, or the phase shift is positive if the target is approaching the radar, while the phase will lag if the target is receding from the radar.

SRF series dual channel Doppler sensor heads offered by Ducommun are designed for **long range** Directional Doppler Radar applications where detection sensitivity is essential.

The simplified block diagram of a Directional Doppler Radar achieved by using Ducommun's dual channel sensor head is shown in the Fig. 3. In a similar manner, a high quality DC power supply for Gunn oscillator bias, a low noise IF amplifier and DSP circuitry are the minimum requirements for a system designer to realize such a radar system.

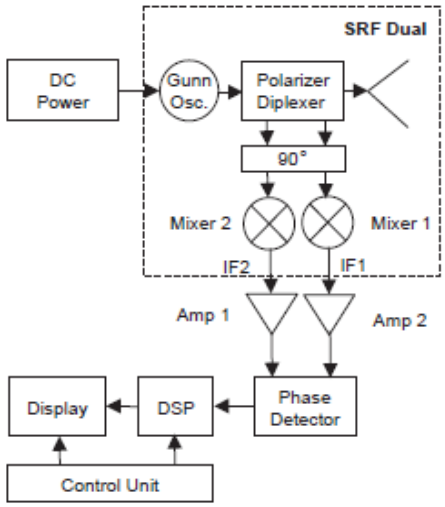

Figure 3. Simplied Directional Doppler Radar

Ranging (Distance) Radar

In many applications, one has to know not only the speed of a moving target, but also the range or distance between the moving or stationary target and the radar. In this case, a Frequency Modulation Continuos Waveform (FMCW) technique may be used in the sensor head to realize the ranging radar.

Implementing the FMCW technique in the sensor head is to replace the fixed tuned oscillator with a Varactor or voltage tuned one.

SRR series dual channel Doppler sensor heads offered by Ducommun are designed for **long range** FMCW Radar application.

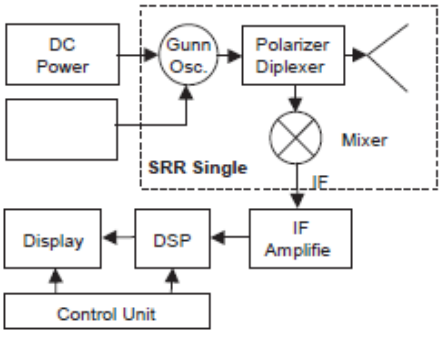

Figure 4. Simplied FMCW Ranging Radar

The simplified block diagram of an FMCW Radar formed by using Ducommun's single channel sensor head is shown in the Fig. 4. In a similar manner, a high quality DC power supply for Gunn oscillator bias, a voltage modulator, a low noise IF amplifier and DSP circuitry are the minimum requirements for a system designer to realize such a radar system. The range information can be extracted from the frequency difference between the transmitted and returned signal at distance R, the signal transit time (ΔT) and the frequency modulation rate (N). The idea is briefly illustrated in the Fig. 5. The detail is explained as follow. At time T1, the signal is transmitted and fed to the mixer at frequency F1. The F1 returned from the target at distance R is received at T2, while the transmitting and LO frequency is F2. With known ramping rate (N), one can find the transit time by using

ΔT = (Ft-Fr)/N,

where **Ft** and **Fr** are the IF frequency at mixer IF port in Hz and **N** is Hz/sec.

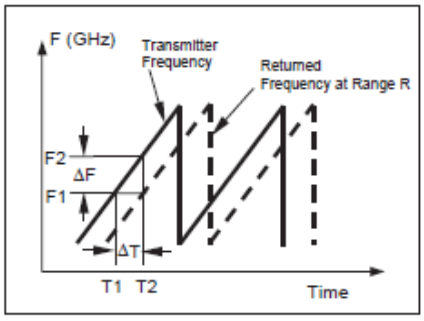

Figure 5. FMCW Radar Frequency vs. Time

Therefore, the range (distance) is given by

R = (ΔT x C)/2

Where **C** is the speed of light, which is 3 x 10^8 (meter/sec).

The range accuracy is governed by the ramp linearity.

From the description above, an FMCW ranging radar can detect not only the stationary target, but also the moving target. Therefore, an FMCW radar is a Doppler Ranging Radar.

Ranging (Distance) Radar with Directional Doppler Feature

With a similar idea, Ducommun's **SRR series** Dual channel sensor head offers ranging capacity with directional features. The simplified block diagram is shown in Fig. 6.

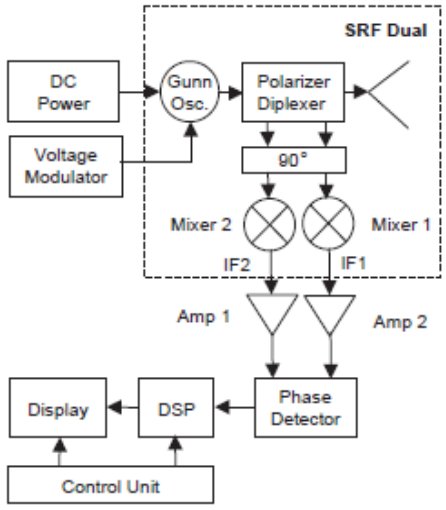

Figure 6. Simplied FMCW Ranging Radar with Directional Doppler Feature

Conclusions

1. Ducommun's **SRF and SRR series** sensor heads offer total solutions for **Long Range** Radar system requirements.

2. Ducommun's **SRF and SRR series** sensor heads can be tailored to various transmitting power levels and antenna gains.

8

References

1. Ahrens, C. Donald, 2003: *Meteorology Today, An Introduction to Weather, Climate, and the Environment, 7th Edition.* Brooks/Cole, Pacific Grove, CA [by] Thomson Learning, Inc. 544 pp.

2. Ducommun Incorporated, 2015: "Doppler Sensor Heads" *Bulletin No. SRF*. Ducommun Inc., Carson, CA. 5 pp. Retrieved from http://ducommun.com/pdf/SRF-Series.pdf

3. Fiorino, 2015 – *personal communication with Dr. Fiorino.*

4. Fiorino, S.T., R.J. Bartell, M.J. Krizo, G.L. Caylor, K.P. Moore, T.R. Harris, and S.J. Cusumano, 2010: "Worldwide uncertainty assessments of ladar and radar signal-to-noise ratio performance for diverse low altitude atmospheric environments" *J. Appl. Remote Sensing*, **Vol 4**, 043533.

5. Fiorino, S.T., R.M. Randall, M.F. Via, and J.L. Burley, 2014: "Validation of a UV-to-RF high-spectral-resolution atmospheric boundary layer characterization tool" *J. Appl. Meteor. Climatol.* **Vol 53**, No. 1, pp. 136-156.

6. Hauser, 2015 – *personal communication with Dr. Hauser.*

7. Hess, M., P. Koepke, and I. Schult, 1998: "Optical properties of aerosols and clouds: the software package OPAC" *Bulletin of the American Meteorological Society*, **Vol 79**, No. 5.

8. Holmes, S. (2012, December 6). Detecting tunnels using seismic waves not as simple as it sounds. Sandia Labs News Release. Retrieved from *https://share.sandia.gov/news/resources/news_releases/seismic_tunnels/#.VYV0zvlViko*

9. MathWorks, Inc. (1994-2015). fft-Fast Fourier transform. MATLAB R2015a Documentation. Retrieved from http://www.mathworks.com/help/matlab/ref/fft.html?searchHighlight=fft

10. Perram, G.P., S.J. Cusumano, R.L. Hengehold, and S.T. Fiorino, 2010: *Introduction to Laser Weapon Systems*. The Directed Energy Professional Society, Albuquerque, NM. 463 pp.

11. Petkie, 2015 – *personal communication with Dr. Petkie.*

12. Petty, G.W., 2006: *A First Course In Atmospheric Radiation, 2nd Edition.* Sundog Publishing, Madison, WI [by] G.W. Petty. 459 pp.

13. Randall, R.M., S.T. Fiorino, M.F. Via, and A.D. Downs, "Validation of Technique to Hyperspectrally Characterize the Lower Atmosphere with Limited Surface Observations," (Proc. SPIE, 8038, 803807) SPIE Defense, Security and Sensing Symposium, Orlando, FL, 25-29 April 2011.

14. Rees, W.G, 2001: *Physical Principles of Remote Sensing, 2nd Edition.* Cambridge University Press, Cambridge, United Kingdom. 343 pp.

15. Reynolds, J.M., 2011: *An Introduction to Applied and Environmental Geophysics, 2nd Edition.* Wiley-Blackwell, West Sussex, UK [by] John Wiley & Sons, Ltd. 696 pp.

16. Senglaub, M., M. Yee, G. Elbring, R. Abbott, and N. Bonal, 2010: "Sensor Integration Study for a Shallow Tunnel Detection System" *Sandia Report, SAND2010-0901.*Sandia National Laboratories, Albuquerque, NM. 43 pp.

17. Via, M.F., S.T. Fiorino, and B.J. Elmore, 2015: "Version 4.0, Patch #7 LEEDR User Guide," Draft Software documentation available through AFIT/CDE, 96 pp.

18. Wallace, J.M. and P.V. Hobbs, 2006: *Atmospheric Science, An Introductory Survey, 2nd Edition.* Elsevier Inc., Oxford, United Kingdom. 483pp.